J. Fluid Mech. (2020), *vol*. 905, A26. © The Author(s), 2020.
Published by Cambridge University Press
doi:10.1017/jfm.2020.726

Methodology for determining coefficients of turbulent mixing model

You-sheng Zhang[1,2], **Zhi-wei He**[1], **Han-song Xie**[1,†], **Meng-Juan Xiao**[1,†] **and Bao-lin Tian**[1,2]

[1]Institute of Applied Physics and Computational Mathematics, Beijing 100094, PR China

[2]Center for Applied Physics and Technology, HEDPS, and College of Engineering, Peking University, Beijing 100871, PR China

(Received 15 February 2020; revised 6 August 2020; accepted 25 August 2020)

The accurate prediction of turbulent mixing induced by Rayleigh–Taylor (R–T), Richtmyer–Meshkov (R–M) and Kelvin–Helmholtz (K–H) instabilities is very important in understanding natural phenomena and improving engineering applications. In applications, the prediction of mixing with the Reynolds-averaged Navier–Stokes (RANS) equation remains the most widely used method. The RANS method involves two aspects, i.e. physical modelling and model coefficients. Generally, the latter is determined empirically; thus, there is a lack of universality. In this paper, inspired by the well-known Reynolds decomposition, we propose a methodology to determine the model coefficients with the following three steps: (i) preset a set of analytical RANS solutions by fully using the knowledge of mixing evolutions; (ii) simplify the differential RANS equations to algebraic equations by imposing the preset solutions to RANS equations; (iii) solve the algebraic equations approximately to give the values of the entire model coefficients. The specific application of this methodology in the widely used K–L mixing model shows that, using the same set of model coefficients determined from the current methodology, the K–L model successfully predicts the mixing evolutions in terms of different physical quantities (e.g. temporal scalings and spatial profiles), density ratios and problems (e.g. R–T, R–M, K–H and reshocked R–M mixings). It is possible to extend this methodology to other turbulence models characterised with self-similar evolutions, such as K-ϵ mixing models.

Key words: turbulent mixing, turbulence modelling

1. Introduction

When a heavy fluid is accelerated by a light fluid, or a shock impacts the interface of two fluids, irregular perturbations present at the interface will develop, causing Rayleigh–Taylor (R–T) (Lord Rayleigh 1882; Taylor 1950; Zhou, Zhang & Tian 2018) instability and Richtmyer–Meshkov (R–M) (Richtmyer 1960; Meshkov 1969; Gao *et al.* 2016, 2017) instability, respectively. Later, triggered by the Kelvin–Helmholtz (K–H) (Helmholtz 1868; Kelvin 1871) instability, which is caused by a shear velocity difference at the interface of two fluids, the instabilities would quickly transition to turbulent

† Email addresses for correspondence: xiehansong19@gscaep.ac.cn; xiao_mengjuan@163.com

mixing (Zhou 2017*a*). In most cases, the shock will further reflect and reshock the mixing zone, accelerating the mixture of two fluids. The R–T, R–M, K–H and reshocked R–M mixings occur widely and, in general, synchronously in several natural phenomena (e.g. supernova explosions Burrows 2000) and engineering applications (e.g. inertial confinement fusion Thomas & Kares 2012). Hence, accurately predicting these mixings is essential (Zhou 2017*b*). For these problems, because of the large Reynolds number, the Reynolds-averaged Navier–Stokes (RANS) simulation remains the widely used method for practical applications (Dimonte & Tipton 2006; Morgan & Greenough 2016; Youngs 2017; Zhou 2017*b*). Without considering numerical methods, the RANS simulation generally involves two steps, namely, (i) establishing a physical model, and (ii) determining the values of the model coefficients. For the former step, several models have been established over the past several decades; we refer the interested reader to Zhou (2017*b*) for a comprehensive review. In this paper we only focus on the latter. Without loss of generality, we choose the basic and widely used two-equation K–L mixing model (Dimonte & Tipton 2006; Kokkinakis *et al.* 2015; Morgan & Greenough 2016; Morgan 2018; Zhang 2018) to demonstrate our new methodology.

Although the K–L model was proposed several decades ago, a relatively full formulation was given only in 2006 by Dimonte & Tipton (2006). After that, this model has been improved to consider shear flows (Morgan & Greenough 2016), enthalpy diffusion and others (Kokkinakis *et al.* 2015). Collecting all the improvements together, the K–L RANS equations, in a coordinate-independent vector form, read as

$$\bar{\rho}_t + \nabla\cdot(\bar{\rho}\tilde{\boldsymbol{u}}) = 0, \tag{1.1}$$

$$(\bar{\rho}\tilde{\boldsymbol{u}})_t + \nabla\cdot(\bar{\rho}\tilde{\boldsymbol{u}}\tilde{\boldsymbol{u}}) + \nabla\bar{p} - \bar{\rho}\bar{\boldsymbol{g}} = -\nabla\cdot\bar{\boldsymbol{\tau}}, \tag{1.2}$$

$$(\bar{\rho}\tilde{E})_t + \nabla\cdot[\tilde{\boldsymbol{u}}(\bar{\rho}\tilde{E}+\bar{p})] - \bar{\rho}\tilde{\boldsymbol{u}}\cdot\bar{\boldsymbol{g}} = D_E + \nabla\cdot[(\mu_t/N_k)\nabla\tilde{K}_f - \bar{\boldsymbol{\tau}}\cdot\tilde{\boldsymbol{u}}], \tag{1.3}$$

$$(\bar{\rho}\tilde{Y}_\alpha)_t + \nabla\cdot(\bar{\rho}\tilde{\boldsymbol{u}}\tilde{Y}_\alpha) = \nabla\cdot[(\mu_t/N_Y)\nabla\tilde{Y}_\alpha], \tag{1.4}$$

$$(\bar{\rho}\tilde{K}_f)_t + \nabla\cdot(\bar{\rho}\tilde{\boldsymbol{u}}\tilde{K}_f) = -\bar{\boldsymbol{\tau}} : \nabla\tilde{\boldsymbol{u}} + \nabla\cdot[(\mu_t/N_k)\nabla\tilde{K}_f] + S_{k_f}, \tag{1.5}$$

$$(\bar{\rho}\tilde{L})_t + \nabla\cdot(\bar{\rho}\tilde{\boldsymbol{u}}\tilde{L}) = \nabla\cdot[(\mu_t/N_L)\nabla\tilde{L}] + C_L\bar{\rho}\sqrt{2\tilde{K}_f} + C_C\bar{\rho}\tilde{L}\nabla\cdot\tilde{\boldsymbol{u}}, \tag{1.6}$$

where $\boldsymbol{g}$ is the volume force (e.g. gravitation). Equations (1.1)–(1.6) describe the evolution of mixed density ρ, velocity $\boldsymbol{u}$, total energy $E \equiv e + \boldsymbol{u}\cdot\boldsymbol{u}/2$ (exclusion of potential energy), mass species $Y_\alpha \equiv \rho_\alpha/\rho$ of the media α, fluctuating/turbulent kinetic energy K_f and turbulent eddy scale L with time t, respectively. The derivation of the equations uses the famous Reynolds decomposition $f \equiv \bar{f} + f'$ and Favre decomposition $f \equiv \tilde{f} + f''$, where '-', '$\sim$', '$'$' and '$''$' denote Reynolds averaged, Favre averaged $\tilde{f} \equiv \overline{\rho f}/\bar{f}$, Reynolds fluctuation and Favre fluctuation, respectively. It is worth emphasizing that the current form of total energy (1.3) exactly takes the same form as that of (17) given in Kokkinakis *et al.* (2015) since $\tilde{E} \equiv \overline{\rho E}/\bar{\rho} = \tilde{e} + \tilde{u}_k\tilde{u}_k/2 + \tilde{K}_f$. However, the form of (1.3) is different from that of (3) given in Kokkinakis, Drikakis & Youngs (2019), in which the potential energy is included. The equation array is solved by coupling with the equation of state (EOS), which establishes relations between inner energy e, pressure p and density ρ, mass fraction Y_α, temperature T. In this paper we only consider the mixing of two ideal gas. Therefore, in correspondence with Livescu (2013), we use the assumptions of iso-temperature (i.e. $T = T_1 = \cdots = T_\alpha$) and partial pressure (i.e. $p = \sum p_\alpha$) to calculate the EOS of the mixture, and the linearly weighted assumption for species (i.e. $f = \sum Y_\alpha f_\alpha$) to calculate the fluid properties of the mixture.

The terms on the right-hand side of (1.1)–(1.6) are the unclosed terms emerging from an ensemble average, which are modelled with the mean fields under various assumptions (e.g. gradient diffusion assumption $-\bar{\rho}\widetilde{\boldsymbol{u}''f''} = (\mu_t/N_f)\nabla\tilde{f}$, where μ_t is the turbulent eddy viscosity and N_f is the non-dimensional model coefficient to be determined). To improve the realisability, the Reynolds stress $\bar{\boldsymbol{\tau}} \equiv \bar{\rho}\widetilde{\boldsymbol{u}''\boldsymbol{u}''}$ is modelled as $\bar{\boldsymbol{\tau}} = C_P\bar{\rho}\tilde{K}_f\boldsymbol{I}$ ($\boldsymbol{I}$ is the unit tensor) in Dimonte & Tipton (2006), Kokkinakis *et al.* (2015) by neglecting the prediction of shear effect, e.g. K–H mixing. To predict shear flow, Morgan & Greenough (2016) recovered the classical closure $\boldsymbol{\tau} = C_P\bar{\rho}\tilde{K}_f\boldsymbol{I} - \mu_t\boldsymbol{s}$ and $\boldsymbol{s} = \nabla\tilde{\boldsymbol{u}} + (\nabla\tilde{\boldsymbol{u}})^{\mathrm{T}} - 2(\nabla\cdot\tilde{\boldsymbol{u}})\boldsymbol{I}/3$, where $\mu_t = C_\mu\bar{\rho}\tilde{L}\sqrt{2\tilde{K}_f}$, although this closure may cause numerical divergence for some problems (Dimonte & Tipton 2006). Considering the importance of K–H mixing in practical applications, Morgan and Greenough's closure of Reynolds stress is adopted in this study. As for the turbulent diffusion of total energy D_E, it was modelled as $D_E = \nabla\cdot[(\mu_t/N_e)\nabla\tilde{e}]$ in Dimonte & Tipton (2006). However, this model would cause an unphysical temperature field, and the model of $D_E = \nabla\cdot[(\mu_t/N_h)\nabla\tilde{h}]$ improved by Kokkinakis *et al.* (2015) would perform better. Here S_{k_f} is the source term of turbulent kinetic energy equation and also the most important term in the K–L model. However, there is a difference in the different papers in both specific expression and numerical implementation (see Dimonte & Tipton (2006), Morgan & Greenough (2016) and Kokkinakis *et al.* (2015) for details). Fortunately, the methodology proposed in this paper, in principle, works for different forms. Therefore, the basic model, $S_{k_f} = \bar{\rho}\sqrt{2\tilde{K}_f}[C_BA_Lg - 2C_D\tilde{K}_f/\tilde{L}]$ with $A_L = C_A\tilde{L}\nabla\bar{\rho}/\bar{\rho}$ is used as an example in this paper. The first part denotes the production term, with specific calculation of C_B given in Kokkinakis *et al.* (2015). The second part denotes the dissipation term, with the improved calculation of the local Atwood number of A_L given in Kokkinakis *et al.* (2015) as well.

In the K–L model there are 11 turbulent model coefficients, i.e. C_A, C_B, C_C, C_D, C_P, C_μ, C_L, N_h (equivalently N_e), N_k, N_L and N_Y. Before the implementation of the RANS model, researchers need to determine their values. Among the model coefficients, only a few can be determined. For instance, assuming that the mass in an eddy is conserved under compression, one can derive $C_C = 1/3$ (Dimonte & Tipton 2006). Again, one can derive $C_P = 2/3$ if the trace of the Reynolds stress tensor does not change before and after modelling. For most model coefficients, however, their values are determined empirically, posteriorly and generally for a specific problem (Dimonte & Tipton 2006; Kokkinakis *et al.* 2015; Morgan & Greenough 2016). Consequently, these model coefficients lack universality and predictability. In addition, because of the lack of a systematic method, researchers often spend considerable time to adjust these model coefficients (Chiravalle 2006), but the corresponding RANS results are often unsatisfactory.

In 2006 significant progress in determining the model coefficients of the K–L model was made by Dimonte & Tipton (2006). In this study, for a one-dimensional (1-D) incompressible mixing problem at a near-unity density ratio, the model coefficients are determined analytically (Dimonte & Tipton 2006). Later, this method was extended to the K–L model considering shear effect (Morgan & Greenough 2016). In this method, the model coefficients were determined by first imposing a set of presupposed analytical evolution profiles to the RANS equation and then solving the RANS equation. However, as discussed later, a part of the presupposed evolutions deviates from the physical evolutions. Moreover, we think that it is this deviation that leads to the unsatisfactory predictions of statistical profiles. To improve prediction, researchers have to go back again to adjust model coefficients (Kokkinakis *et al.* 2015; Morgan & Greenough 2016). In table 1 we list the values of 11 model coefficients used in different papers (Dimonte & Tipton 2006;

Kokkinakis *et al.* 2015; Morgan & Greenough 2016). From this table and references (Dimonte & Tipton 2006; Kokkinakis *et al.* 2015; Morgan & Greenough 2016), we can find that (i) for the same mixing problems (e.g. R–T mixing), different model coefficients have been used by different authors (Dimonte & Tipton 2006; Kokkinakis *et al.* 2015); (ii) for the different mixing problems, different coefficients have been used by the same authors (Dimonte & Tipton 2006); (iii) for the same problems and same authors, different model coefficients have been used for cases with different density ratios (Kokkinakis *et al.* 2015), different quadratic growth coefficients (Morgan & Greenough 2016) and different configurations of reshocked R–M mixing (Dimonte & Tipton 2006). For example, to predict the mixing with different growth law caused by different initial perturbations, most model coefficients in Morgan & Greenough (2016) differ by a factor as large as seven. However, the authors did not document the detailed procedure about how to adjust these model coefficients with Dimonte and Tipton's method. In fact, because of the unsatisfactory quantification of the shape of spatial profiles, we find that it is very difficult to reproduce the evolution of both time scalings (e.g. mixing width and maximum turbulent kinetic energy) and spatial profiles (e.g. profiles of species and turbulent kinetic energy) at the same time by adjusting these model coefficients with this method.

Therefore, it is necessary to develop a systematic methodology to guide the adjustment of turbulence model coefficients. In this paper we devote to developing such a methodology with anticipation that (i) the model coefficients can accurately predict the evolution of both time scalings and spatial profiles, as both of them are important for engineering applications (Kokkinakis *et al.* 2015); (ii) the model coefficients are independent of density ratios R since R varies widely and quickly in practical applications; (iii) the model coefficients are the same for R–T, R–M, K–H and reshocked R–M mixing problems as the four mixing problems often coexist in practical applications (Zhou 2017*b*).

This paper is structured as follows. In order to make it easier for readers to understand this paper, some basic knowledge is first given in § 2, including mixing laws in § 2.1, RANS problems in § 2.2 and RANS implementation in § 2.3. For experts working in the mixing field, he or she can skip § 2 and read directly from § 3 for the current methodology. In § 3 we will first present a general logic of the new method in § 3.1, followed by detailed derivations of constraint relations among different model coefficients in § 3.2. Applications of these constraint relations and current methodology are given in § 4. Firstly, based on the constraint relations derived in § 3.2, detailed procedures to determine the values of model coefficients by providing data of a specific R–T problem will be given as an example in § 4.1. Next, in § 4.2, we have validated that, using the set of common model coefficients determined in § 4.1, the K–L model has successfully reproduced the mixing evolution in terms of different physical quantities (e.g. temporal scalings and spatial profiles), density ratios and problems (e.g. R–T, R–M, K–H and reshocked R–M mixings). Finally, discussions and conclusions are provided in §§ 5 and 6, respectively.

2. Background knowledge

2.1. *Mixing laws*

In this section we will briefly document the basic knowledge about the mixing evolution of four kinds of mixing problems. As for the mixing evolution, we think it can be described in three levels (Zhang *et al.* 2020): (i) mixing width, (ii) mean profiles (Ruan *et al.* 2019) and (iii) flow structures. For practical applications, the most important thing is to predict the evolution at the first two levels as, with this information, one can predict the first useful quantity of mixed mass (Zhou, Cabot & Thornber 2016; Zhang *et al.* 2020). This may

https://doi.org/10.1017/jfm.2020.726 Published online by Cambridge University Press

Mixing problems	C_C	C_D	C_P	C_L	N_k	N_L	N_Y	$N_{e,h}$	C_A	C_B	C_μ
R–T, R–M and reshocked R–M[a]	1/3	1.25	2/3	1	1	0.5	1	1	2	0.84	1
R–T[b] $R = 3:1$	1/3	0.92	2/3	1	1.5	0.125	1.125	1.125	2	0.86	0.70
$R = 20:1$	1/3	0.90	2/3	1	1.5	0.125	1.125	1.125	2	0.97	0.68
Cylinder[c] $\alpha_b = 0.06$	1/3	0.35	2/3	1	1	0.5	1	1	2	0.84	1
$\alpha_b = 0.025$	1/3	0.35	2/3	0.28	0.14	0.07	0.14	0.14	4.47	0.55	0.2
Current paper[d] $\alpha_b = 0.05$	1/3	0.20	2/3	0.19	0.43	0.04	0.35	$0.35/\gamma, 0.35$	11.2	0.76	1.19[e]

TABLE 1. The K–L model coefficients used in previous literature and in this paper.

[a]Only the standard model coefficients are listed. For the reshocked R–M mixing experiment conducted by Poggi, Thorembey & Rodriguez (1998), different model coefficients have been used (see Dimonte & Tipton (2006) for details).

[b]For the problem with different density ratios R, there is a slight difference in some model coefficients (Kokkinakis *et al.* 2015).

[c]The corresponding model coefficients (Morgan & Greenough 2016) are determined by using the classical R–T mixing problem with different quadratic growth coefficients of the bubble mixing zone, i.e. α_b.

[d]In the current paper we do not think there should exist a set of universal model coefficients for all problems. In contrast, our methodology implies that the values of the model coefficients are associated closely with a specific problem. For example, the quadratic growth coefficient α_b in R–T mixing evolving from long- and short-wave perturbations approximately takes the values of 0.05 and 0.025, respectively, according to Youngs (2013). Correspondingly, different sets of model coefficients should be used for different α_b. Here, we only list the values of model coefficients corresponding to $\alpha_b = 0.05$.

[e]This set of model coefficients is slightly different from the one used in our previous work by Xiao, Zhang & Tian (2020), explained later in § 3.2. However, this change is proven to have marginal influence on the final results of the previous work (Xiao *et al.* 2020).

partially explain why RANS simulation, in comparison with large eddy simulation (LES) and direct numerical simulation (DNS), remains the most popular method in practical applications. Following this logic, in this section we only present the basic knowledge about mixing at the first two levels, which will be fully used in deriving the constraint relations of model coefficients in § 3.

We begin by giving a basic definition on mixing width. For either R–T or R–M mixing, the mixing region consists of a bubble mixing zone (formed by the bubble structures when light fluid penetrates into heavy fluid) and a spike mixing zone (formed by the spike structures when heavy fluid penetrates into light fluid). The mixing width is defined as the distance between the front part of the spikes and that of the bubbles and is often quantified with the aid of volume species profiles $\tilde{\phi}_1$ (of heavy fluid), which relates with mass species $\tilde{\phi}_1$ (of heavy fluid) (Thornber *et al.* 2010; Kokkinakis *et al.* 2019) as

$$\tilde{\phi}_1 = \tilde{Y}_1/[\tilde{Y}_1 + (1 - \tilde{Y}_1)R], \tag{2.1}$$

where $R \equiv \rho_1/\rho_2$ is the density ratio of heavy fluid ρ_1 to light fluid ρ_2, and $\tilde{Y}_1$ is the Favre-averaged mass fraction of heavy fluid. In the literature the following definitions of mixing width are frequently used and widely accepted: (i) species-truncated mixing width H, which is defined as the distance between the locations of $\tilde{\phi}_1 = \psi$ and $\tilde{\phi}_1 = 1 - \psi$, with $\psi = 0.01$ (Cook & Cabot 2006), 0.05 (Akula & Ranjan 2016; Roberts & Jacobs 2016) and other values; (ii) species-integrated mixing width W, which is defined as the following integration, along the mixing evolution direction x (Anderews & Spalding 1990; Thornber *et al.* 2010):

$$W = \int_{-\infty}^{+\infty} \tilde{\phi}_1(1 - \tilde{\phi}_1)\,\mathrm{d}x. \tag{2.2}$$

In terms of measurement, it is more straightforward to describe the mixing width with the first definition. Unfortunately, truncated by two concentration points, this definition may produce a non-smooth evolution curve $H(t)$ (Dimonte *et al.* 2004). The second definition can significantly improve this smoothness by using the global concentration information (Youngs 2013), and, for a given R, the latter differs from the former by just an approximate constant factor (Dimonte *et al.* 2004). Therefore, the latter has been used widely in the literature, especially in simulations. In this paper, for convenience in comparisons, both definitions are used, and $\psi = 0.01$ is used for the first definition. For K–H mixing, the mixing develops perpendicularly towards the convection direction y, i.e. along the x direction. The following definition produces a non-dimensional velocity profile varying smoothly from 0 to 1:

$$\tilde{v}_{non\text{-}dim}(x) \equiv [\tilde{v}(x) - \tilde{v}_{low}]/[\tilde{v}_{high} - \tilde{v}_{low}], \tag{2.3}$$

where $\tilde{v}_{low}$ and $\tilde{v}_{high}$ denote the lower and higher convection velocities of two fluids, respectively (Brown & Roshko 1974; Slessor, Zhuang & Dimotakis 2000). Similar to the first definition of R–T and R–M mixing models, the mixing width H in K–H mixing can be defined by replacing $\tilde{\phi}_1$ with $\tilde{v}_{non\text{-}dim}$.

Classical R–T mixing. For the classical R–T turbulent mixing problem with constant acceleration g, the mixing width grows quadratically with time t as

$$h_{b,s} = \alpha_{b,s} A g t^2, \tag{2.4}$$

where subscripts b and s denote the spike mixing zone and bubble mixing zone, respectively. Here $h_{b,s}$ is defined as the distance between the front part of bubbles/spikes

and the initial unperturbed interface, respectively, and $H \equiv h_b + h_s$. The Atwood number $A \equiv (\rho_1 - \rho_2)/(\rho_1 + \rho_2)$ is a non-dimensional density ratio varying from 0 to 1. We denote by α the quadratic growth coefficient. Now, it is clear that the value of α sensitively depends on the initial perturbations (Ramaprabhu, Dimonte & Andrews 2005; Banerjee & Andrews 2009; Youngs 2013). For the perturbation involving only short waves, α tends to take the universal lower limit of 0.025 (Dimonte *et al.* 2004; Ramaprabhu *et al.* 2005). In contrast, if the perturbation involves long waves, the corresponding α proportionally depends on the amplitude of the initial perturbation, without the widely accepted and validated formula (Dimonte 2004; Ramaprabhu *et al.* 2005; Mueschke & Schilling 2009; Livescu, Wei & Petersen 2011; Youngs 2013). Up to now, the lowest and largest α observed in simulations is 0.02 (Olson & Jacobs 2009; Cabot & Zhou 2013) and 0.12 (Youngs 2013), respectively. In contrast, α in most experiments is in the range of 0.05∼0.07 (Read 1984; Youngs 1989; Dimonte & Schneider 2000). Rayleigh–Taylor mixing is a process that converts potential energy to kinetic energy and dissipation heat. Previous experiments and numerical simulations show that the ratio of the generated kinetic energy to the converted potential energy ($\Delta E_k/\Delta PE$) approximates 0.5 (Dimonte *et al.* 2004; Cook & Cabot 2006).

Classical K–H mixing. For the K–H turbulent mixing problem, the total mixing width $H(t)$ grows linearly with time t as (Brown & Roshko 1974)

$$H(t) = \alpha_{KH} \Delta \tilde{v} t, \tag{2.5}$$

where $\Delta \tilde{v}$ is the shear velocity difference and α_{KH} is a linear growth coefficient. The value of α_{KH} depends on many factors, such as the density ratio of two fluids and the convection Mach number (see Slessor *et al.* (2000) for a comprehensive review). For a uniform density flow, Brown & Roshko (1974) observed that $\alpha_{KH} \approx 0.18$.

Classical and reshocked R–M mixing. For the classical R–M turbulent mixing problem with impulsive acceleration or shock, the mixing width is a power function of time t (Dimonte 2004), i.e.

$$h_{b,s}(t) = h(0)(1 + t/t_c)^{\theta_{b,s}}, \tag{2.6}$$

where $t_c \equiv \theta_{b,s} h(0)/\dot{h}(0)$ is a characteristic time determined only by initial mixing width $h(0)$, initial growth speed $\dot{h}(0)$ and power index $\theta_{b,s}$. The subscripts b and s denote the spike mixing zone and the bubble mixing zone, respectively. The total mixing width is $H \equiv h_b + h_s$. Similar to R–T mixing, the evolution of $H(t)$ in R–M mixing also sensitively depends on the initial perturbations (Thornber *et al.* 2010). Up to now, the value of θ_b is observed varying widely from $0.19 \sim 0.67$ (Liu & Xiao 2016; Krivets, Ferguson & Jacobs 2017; Zhou 2017*b*), with $\theta_s \sim \theta_b$ and $\theta_s > \theta_b$ in problems with small and large R, respectively (Dimonte & Schneider 2000). With initial perturbations generated by a short period of R–Tmixing, the impulsive accelerated linear electric motor (LEM) R–M experiments obtained $\theta_b \approx 0.25$ for all R (Dimonte & Schneider 2000). Moreover, in several applications, the shock may be reflected, reshocking the R–M mixing zone and resulting in a rapid growth and complex variation of $H(t)$ (Vetter & Sturtevant 1995; Poggi *et al.* 1998). Our recent work (Li *et al.* 2019*a*,*b*) shows that, in this complex flow the entire evolution of $H(t)$ can be described by combining (i) the R–T effect caused by acceleration history, (ii) the R–M effect inherited from previous turbulent mixing, and (iii) the stretching/compression effect caused by waves.

It is necessary to discuss some common characteristics of the mentioned mixing problems. Firstly, after the mixing has been fully developed, most statistical profiles evolve self-similarly along both the temporal and spatial directions. In other words, the statistical

profiles at different times can be collapsed together after rescaling the spatial coordinate and amplitude. For example, the profiles of $\tilde{\phi}_1(x)$ (R–T and R–M) and $\tilde{v}_{non\text{-}dim}(x)$ (K–H) can be collapsed by only rescaling the spatial coordinate. Again, the profiles of the turbulent kinetic energy $\tilde{K}_f$ can be collapsed at different times by rescaling both the spatial coordinate and amplitude. This property of self-similarity makes it possible to express the evolution of the statistical profile $f(\boldsymbol{x}, t)$ in the form of separated temporal–spatial variables,

$$f(\boldsymbol{x}, t) = f_{ref} + f(t) f(\boldsymbol{x}_{non\text{-}dim}), \tag{2.7}$$

where f_{ref} denotes a reference profile without considering the temporal and spatial evolutions, $\boldsymbol{x}$ denotes the dimensional spatial coordinate and $\boldsymbol{x}_{non\text{-}dim} \equiv \boldsymbol{x}/\ell$ denotes a non-dimensional spatial coordinate rescaled by a characteristic length scale ℓ. For the currently investigated mixing problems, the property of self-similarity implies that the mixing width $H(t)$ is a natural length scale. As explained in § 3.2, the length scale is chosen as $\ell(t) \sim H(t)/2 \sim h(t)$ in this paper.

2.2. *RANS problems*

To check the effectiveness of model coefficients derived from the method documented in this paper, some basic mixing problems are designed for tests. Firstly, we describe the test problems used in RANS simulations in this section.

Classical R–T mixing. For the classical R–T mixing problem, a 1-D configuration similar to Kokkinakis *et al.* (2015) is used. In this configuration the heavy and light fluids are placed on the computational domain of $[-8, 0]$ cm and $[0, 20]$ cm, respectively. A uniform gravity acceleration of g is imposed along the $+x$ direction, and the value of g is set to meet $Ag = 1$ cm s^{-2}. In this paper two cases of $A = 0.5$ ($R = 3:1$) and $A = 19/21 \approx 0.9$ ($R = 20:1$) are simulated. A total of 2000 grids are distributed uniformly across the computational domain. Two compressible ideal gases with adiabatic exponent $\gamma = 1.4$ and molecular weight $M = 0.0288$ kg mol^{-1} are used to approximate incompressible mixing. For ideal R–T mixing, the initial flow field should be in a state of hydrostatic and thermodynamic equilibrium. The former implies $\boldsymbol{u} = 0$, and the latter implies $T =$ constant. For incompressible R–T mixing, however, only the first constraint is strictly adopted in the literature (Dimonte *et al.* 2004), and the second constraint is generally replaced by other constraints since the thermodynamics has little influence on the corresponding evolution. In this paper the frequently used assumption of an adiabatic process (i.e. $p/\rho^{\gamma} =$ constant) is adopted (Dimonte *et al.* 2004). Combining this assumption and the EOS of an ideal gas, we can integrate the momentum equations with constraint of $\boldsymbol{u} = 0$ to derive the initial profiles of density and pressure as

$$\bar{\rho}_0(x) = \begin{cases} \bar{\rho}_{0H}\left[1 + \dfrac{\gamma - 1}{\gamma}\dfrac{\bar{\rho}_{0H}}{\bar{p}_{0I}} g(x - x_I)\right]^{1/(\gamma-1)}, & x < x_I \\ \bar{\rho}_{0L}\left[1 + \dfrac{\gamma - 1}{\gamma}\dfrac{\bar{\rho}_{0L}}{\bar{p}_{0I}} g(x - x_I)\right]^{1/(\gamma-1)}, & x \geq x_I \end{cases}, \tag{2.8}$$

$$\bar{p}_0(x) = \begin{cases} \bar{p}_{0I}\left[1 + \dfrac{\gamma - 1}{\gamma}\dfrac{\bar{\rho}_{0H}}{\bar{p}_{0I}} g(x - x_I)\right]^{\gamma/(\gamma-1)}, & x < x_I \\ \bar{p}_{0I}\left[1 + \dfrac{\gamma - 1}{\gamma}\dfrac{\bar{\rho}_{0L}}{\bar{p}_{0I}} g(x - x_I)\right]^{\gamma/(\gamma-1)}, & x \geq x_I \end{cases}, \tag{2.9}$$

where $x_I = 0$ is the interface position, the subscript 0 denotes the interface (throughout this paper), $\bar{p}_{0I}$ is the interface pressure, $\bar{\rho}_{0H}$ and $\bar{\rho}_{0L}$ denote the density located at $x = 0^-$ (the side of heavy fluid) and $x = 0^+$ (the side of light fluid), respectively. The density $\bar{\rho}_{0L}$ is fixed as 1 g cm^{-3}, and $\bar{\rho}_{0H}$ is correspondingly set as $\bar{\rho}_{0H} = \bar{\rho}_{0L}(1 + A)/(1 - A)$ g cm^{-3}. The value of $\bar{p}_{0I}$ will influence the shape of the density profile, and a larger value of $\bar{p}_{0I}$ would lead to a flatter density profile to approach the incompressible limit. Therefore, in this study a large value, 6000 g cm^{-1} s^{-2}, is used to guarantee that the variation of A in the entire process is smaller than 1 %. The velocity is initialised as zero across the whole field. The mass fraction of heavy fluid $\tilde{Y}_1(x)$ is set as 1 for $x < x_I$ and 0 for $x \geq x_I$. For the K–L model, inside the grids near the interface ($|x| \leq \Delta x$, Δx is the mesh scale), the initial turbulent kinetic energy $\tilde{K}_f(0)$ is set as $\tilde{K}_f(0) = CAg\tilde{L}(0)$ by a simple dimensional analysis, where C is an arbitrary constant and set as $C = 4$; the initial length scale $\tilde{L}(0)$ is set as $\tilde{L}(0) = 1 \times 10^{-3}$ (Kokkinakis *et al.* 2015). Outside the interface region ($|x| \leq \Delta x$), either $\tilde{K}_f$ or $\tilde{L}$ is initialised as zero.

Classical K–H mixing. We use a two-dimensional configuration given in Chiravalle (2006) to check the application of the current method for K–H mixing problems. In this configuration, a rectangular computational domain of $[-1.5, 1.5] \times [0, 0.016]$ cm is used. The flow field is initialised with a uniform density (ρ) of 1 g cm^{-3} and pressure (p) of 0.0127 Mbar. The velocity and mass fractions are set as $(\tilde{u}, \tilde{v}) = (0, 0.078$ cm μs$^{-1})$ and $\tilde{Y}_1(x) = 0$ for the domain of $x < 0$ cm; $(\tilde{u}, \tilde{v}) = (0, 0.109$ cm μs$^{-1})$ and $\tilde{Y}_1(x) = 1$ for others. The fluid is an ideal gas with a molecular weight $M = 0.0288$ kg mol^{-1} and $\gamma = 1.4$. Nearby the interface ($|x| \leq \Delta x$), $\tilde{K}_f(0)$ and $\tilde{L}(0)$ are set as $\tilde{K}_f(0) = 4 \times 10^{-5}$ cm μs^{-2} and $\tilde{L}(0) = 1 \times 10^{-2}$ cm. In other regions, both are set as 0.

Classical and reshocked R–M mixings. We design a 1-D configuration by referring to the 85th experiment conducted in Vetter & Sturtevant (1995) to confirm the application of the current method for both classical and reshocked R–M mixing problems. In the R–M mixing problem, no matter from which directions the shock wave impacts the interface, mixing will occur. Hence, we introduce a signed $A \equiv (\rho_R - \rho_L)/(\rho_R + \rho_L)$ to characterise the configuration, where ρ_R and ρ_L denote the initial densities at the right and left of the interface located at $x = 0$. Consequently, the positive (negative) A means that the first shock impacts the interface from light (heavy) fluid to heavy (light) fluid. Based on this definition, the following initialisation is used for classical and reshocked R–M mixings.

Classical R–M mixing with $A = \pm 0.1, \pm 0.5, \pm 0.9$:

$$(\bar{\rho}, \tilde{u}, \bar{p}, \gamma, M, \tilde{Y}) = \begin{cases} (0.521379, 23.5498, 565.417, 1.4, 0.0288, 1), & -221 \leq x < -1, \\ (0.28, 0, 230, 1.4, 0.0288, 1), & -1 \leq x \leq 0, \\ (0.28(1+A)/(1-A), 0, 230, 1.4, 0.0288, 1), & 0 < x \leq 301. \end{cases} \tag{2.10}$$

Reshocked R–M mixing with $A = 0.67$ (the shock firstly sweep the interface from light fluid to heavy fluid, Vetter & Sturtevant 1995; Tritschler *et al.* 2014; Thornber, Groom & Youngs 2018):

$$(\bar{\rho}, \tilde{u}, \bar{p}, \gamma, M, \tilde{Y}) = \begin{cases} (0.521379, 23.5498, 565.417, 1.4, 0.0288, 1), & -61 \leq x < -1, \\ (0.28, 0, 230, 1.4, 0.0288, 1), & -1 \leq x \leq 0, \\ (1.4, 0, 230, 1.093, 0.146, 0), & 0 < x \leq 61. \end{cases} \tag{2.11}$$

Reshock R–M mixing with $A = -0.67$ (the shock firstly sweeps the interface from heavy fluid to light fluid; Poggi *et al.* 1998):

$$(\bar{\rho}, \tilde{u}, \bar{p}, \gamma, M, \tilde{Y}) = \begin{cases} (0.28, 0, 245, 1.4, 0.0288, 1), & -30 \le x < 0, \\ (1.4, 0, 245, 1.093, 0.1460), & 0 \le x \le 0.1, \\ (2.806, -10.05, 527.1, 1.093, 0.146, 0), & 0.1 < x \le 20, \end{cases} \tag{2.12}$$

where M is the molecular weight of the ideal gas, and the units of ρ, u, p, M and x are kg m^{-3}, cm ms^{-1}, 10^2 Pa, kg mol^{-1} and cm, respectively. For all cases, the quantities after the shock are calculated from the 1-D shock wave relation by using the shock Mach number from the literature. For the reshocked R–M mixing with $A = -0.67$, the original literature did not mention anything about pressure. In this paper the pressure is set to best match the two times that the reflected compression wave and the rarefaction wave interact with the mixing zone at $t = 1.15$ ms and $t = 1.9$ ms, respectively. For the reshocked R–M mixings with $A = 0.67$ and $A = -0.67$, the wall is located at the right and left end of the computational domain, respectively, and a corresponding wall-reflected boundary condition is used. For the others, a non-reflecting boundary condition is imposed. As for the grids, a uniform grid with $\Delta x = 0.06$ cm is used for reshocked R–M mixing with $A = 0.67$ and $\Delta x = 0.1$ cm for others. As for the initialisation of $\tilde{K}_f$ and $\tilde{L}$, only $\tilde{L}(0)$ is specified close to the interface ($|x| \le \Delta x$). It is worth mentioning that the value of $\tilde{L}(0)$ associates closely with the grid resolution. In this paper we determine the initial value of $\tilde{L}(0)$ by matching the mixing width of RANS results to that of corresponding experiments. Specifically, $\tilde{L}(0)$ is set as 0.05, 0.06 and 0.046 cm for classical R–M mixing, reshocked R–M mixing with $A = 0.67$ and reshocked R–M mixing with $A = -0.67$, respectively.

2.3. *RANS implementation*

Due to the introduction of many additional closure terms, we find that correctly implementing the K–L model is not a trivial matter. However, a comprehensive discussion of the numerical implementation of the K–L model is beyond the scope of the current paper and will be addressed in other studies. In this paper we brief the points that need special attention.

Firstly, we discuss additional constraints on $\tilde{K}_f$ and $\tilde{L}$. In the implementation of the K–L model, to avoid the termination of calculation caused by $\tilde{K}_f$ and $\tilde{L}$, additional constraints of $\tilde{K}_f = \max\{\varepsilon_{K_f}, 0\}$ and $\tilde{L} = max\{\varepsilon_L, 0\}$ are imposed to exclude the appearance of 0/0 and avoid the unphysical negative value, where ε_{K_f} and ε_L are infinitesimal quantities nearing zero. As for the specific value of ε_{K_f} and ε_L, they are set by further considering the start-up process. During the start-up stage, the magnitude of the source term of the turbulent kinetic energy equation (i.e. S_{k_f}) contributes dominantly to the evolution of $\tilde{K}_f$. According to (1.5), a large and native S_{k_f} may lead to the appearance of negative $\tilde{K}_f$. It is really possible that this situation happens during the start-up stage, as $S_{k_f} \sim -\tilde{K}_f^{3/2}/\tilde{L} \sim -\varepsilon_{K_f}^{3/2}/\varepsilon_L$ and both ε_{K_f} and ε_{K_f} are infinitesimal values. The values of ε_{K_f} and ε_L can be set by analysing (1.5). If we neglect all terms on the right-hand side of (1.5) except the dissipation term, under the assumption of constant $\bar{\rho}$, the equation can be simplified to

$$\mathrm{D}\sqrt{\tilde{K}_f}/\mathrm{D}t = -\sqrt{2}C_D\tilde{K}_f/\tilde{L}, \tag{2.13}$$

where D is the material derivative. Integrating (2.13) with an explicit method gives $\sqrt{\tilde{K}_f} = \sqrt{\tilde{K}_f(0)}[1 - \sqrt{2}C_D\sqrt{\tilde{K}_f(0)}/\tilde{L}(0)\Delta t]$, where Δt denotes the time step. Hence, to avoid the occurrence of negative $\tilde{K}_f$ at the start-up stage, we can impose $\sqrt{\varepsilon_{K_f}} \ll \varepsilon_L$ to guarantee that $\sqrt{\tilde{K}_f(0)}/\tilde{L}(0) \ll 1$. Based on these analyses, in this paper we set $\varepsilon_{K_f} = 1 \times 10^{-40}$ and $\varepsilon_L = 1 \times 10^{-16}$.

Secondly, we discuss numerical methods used to solve governing equations. Based on a lot of numerical practices, we find that it is difficult to correctly implement the K–L model, especially for the mixing problem involving strong discontinuity and strong shear. When a strong discontinuity occurs in the mixing region (e.g. shock), the solution of closure terms involving a spatial gradient (e.g. $\partial_{x_i} f$) would easily produce non-physical numerical oscillations and is sensitive to the grid resolution (Moran-Lopez & Schilling 2013), resulting in incorrect and non-convergent results. Besides this, compared with the classical K–L model (Dimonte & Tipton 2006; Kokkinakis *et al.* 2015), the modelling of shear effect in the current model sets higher requirements on the stability of numerical methods, time step and grid resolutions. In practice, to explore applicable numerical schemes, we first implement the numerical scheme given in Kokkinakis *et al.* (2015) without considering the shear effect. Using the same grid resolution (Kokkinakis *et al.* 2015), we reproduce the R–T results. However, when the shear effect is included, we find that a convergent result can be obtained only with a shorter time step, a higher grid resolution and a longer time for transition to the self-similar stage. Moreover, when the shock of R–M is involved, we find that it is very difficult to obtain a physical evolution because it is difficult to obtain a numerical solution without any unphysical numerical oscillation, especially for mixing problems involving multi-materials (i.e. the specific heat ratio $\gamma_1 \neq \gamma_2$) or shock. Consequently, unphysical and non-convergent results may be produced because of the numerical oscillations. Therefore, to correctly implement the K–L model, the first general principle is to avoid any numerical oscillation by carefully selecting numerical methods. Under this principle, for mixing problems of R–T, R–M, K–H and reshocked R–M considered in this paper, we find that it is difficult to obtain satisfactory results with unified numerical schemes. To explore satisfactory numerical schemes, a lot of numerical combinations have been tested. The main numerical aspects analysed in this paper include a difference scheme and Riemann solver used to calculate the convection terms, and the numerical technique to calculate the local Atwood number A_L in S_{k_f}. For all analyses, the time term is advanced by the third Runge–Kutta method, with a very small Courant–Friedich–Lecy stability of 0.05 to improve the stability. To reduce the numerical dissipation, a low-Mach modification number (Thornber *et al.* 2008*a*,*b*) is used during the reconstruction of the half-point flux of convection term, and the second-order central difference scheme is applied to calculate the turbulent diffusion term. In table 2 we list the satisfactory numerical combinations for different problems, in the form of 'difference scheme + Riemann solver'. In this table MMD2 and MUSCL5 denote the conventional total variation diminishing (TVD) (Harten 1997; Sweby 1984) scheme with second-order min-mod limiter and improved fifth-order limiter (Kim & Kim 2005*a*,*b*), respectively. The HLL (Harten, Lax and van Leer (Harten, Lax & Leer 1983)) Riemann solver for contact discontinuity (HLLC) (Toro, Spruce & Speares 1994) is used to estimate the inter-cell numerical flux with pressure-based wave speed. We find that the numerical combinations listed in table 2 can effectively prevent unphysical oscillations for problems involving either shock or multi-material, although the numerical mechanism needs further exploration in the future. From this table we find that the combination of TVD scheme

Mixing problems	Numerical schemes
Classical R–T	$A = 0.1$: MUSCL5/MMD2 + HLL
Classical R–T	$A = 0.3/5/7/9$: MUSCL5/MMD2 + HLLC
Classical K–H	MUSCL5/MMD2 + HLL
Classical R–M	$A = \pm 0.1/3/5/7, -0.9$: MUSCL5/MMD2 + HLLC
Classical R–M	$A = 0.9$: MUSCL5 + HLL, MMD2 + HLLC
Reshocked R–M ($A = 0.67$)	MUSCL5/MMD2 + HLLC
Reshocked R–M ($A = -0.67$)	MUSCL5 + HLLC, MMD2 + HLLC

TABLE 2. Numerical schemes used for problems investigated in this paper.

(either MMD2 or MUSCL5) + HLLC works for most problems that are consistent with Kokkinakis *et al.* (2015). However, this combination does not always work for all problems. In this paper the RANS results are obtained with the underlined numerical combinations, in which the fifth-order difference scheme, instead of the second-order MMD2, is used to accelerate the convergence and to reduce the number of grids. Finally, the local Atwood number A_L is calculated with the improved scheme (Kokkinakis *et al.* 2015), not with the original scheme (Dimonte & Tipton 2006). However, the method used to evaluate the value of half-point density is different from that given in Kokkinakis *et al.* (2015). In this paper the value of half-point density is directly 'interpolated' with the second-order central difference scheme, in contrast to that of 'reconstruction' with the TVD scheme and van Leer limiter in Dimonte & Tipton (2006) and Kokkinakis *et al.* (2015) (see details in literature).

All the RANS simulations are implemented in the code of finite difference for compressible fluid dynamics (CFD^2) developed by You-sheng Zhang *et al.* since 2016. The MPI-based parallel CFD^2 is devoted to providing a unified framework for solving the partial difference equation array. The CFD^2 integrates several numerical schemes and solvers and is particularly effective in solving problems involving multiscale (e.g. turbulence), multi-materials (e.g. interface instability) and multi-physics (e.g. elastoplasticity, flow and others).

3. Current methodology

3.1. *Overall ideas*

Before the formal presentation of the new methodology, we briefly review previous methods in determining the model coefficients of the turbulent mixing model using figure 1.

In practical applications, the effective method, which is also used widely, is to adjust model coefficients to match several conducted (physical or numerical) experiments, symbolized as nodes I-V in figure 1. Specifically, as shown by the dashed arrows in figure 1, for a specific flow problem, researchers can obtain a corresponding RANS solution $\boldsymbol{F}_{RANS}$ (node III) by first providing a set of specific model coefficients (node I) and then solving the RANS equation set (1.1)–(1.6) noted as $\partial \boldsymbol{G}(\boldsymbol{F}_{RANS}) = \boldsymbol{0}$ (node II). Obviously, researchers expect that the RANS solution $\boldsymbol{F}_{RANS}$ can approach the physical evolution $\boldsymbol{F}_{phy}$, in terms of temporal scalings and statistical profiles (node IV). To realise such a goal, researchers must artificially adjust these model coefficients many times before obtaining a satisfactory $\boldsymbol{F}_{RANS} \approx \boldsymbol{F}_{phy}$ (node V). What is worse, as these adjustments are

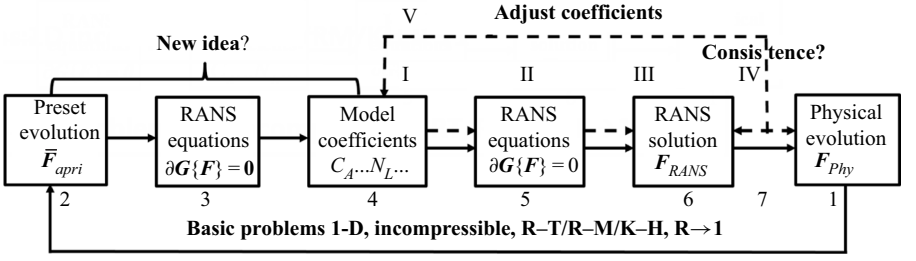

FIGURE 1. The schematic demonstration of the traditional (dashed arrows, nodes I-V) and current (solid arrows, nodes 1–7) methods in determining the model coefficients of the turbulent mixing model.

artificial, it is generally difficult to obtain a set of model coefficients producing satisfactory temporal scalings and statistical profiles at the same time and for different problems. After calibrating a set of model coefficients with some conducted experiments, these model coefficients are then assumed to work for other problems. As the model coefficients are determined empirically in this method, the degree of confidence of RANS prediction is questionable, especially for extrapolation problems.

To avoid the empirical property of the aforementioned method, a systematically analytical method was developed by Dimonte & Tipton (2006) for the K–L mixing model, symbolized as nodes 1–7 in figure 1. In this method, by presetting a specific and special form of $\boldsymbol{F}_{RANS}$ (node 2) with the knowledge of mixing evolutions (node 1), the authors analytically solved the RANS equation array by fully using the self-similar property of mixing evolution (node 3). Then a set of algebraic constraint relations about these model coefficients is derived. Jointly solving the constraint relations gives the values of all model coefficients (node 4). Solving the RANS equation with these model coefficients (node 5), researchers can obtain the RANS evolution (node 6). Obviously, the best result is that the RANS solutions can asymptotically approach the physical evolution (node 7), and, thus, the seven nodes consist an ideal cycle.

Dimonte and Tipton's method has been widely accepted and also generalized in the continued study (Morgan & Greenough 2016). Unfortunately, the recent study implies that this method cannot properly reproduce physical profiles (Kokkinakis *et al.* 2015). For example, the $\tilde{K}_f$ profile predicted by these model coefficients is parabolic, as assumed in the specific form of $\boldsymbol{F}_{RANS}$ (Dimonte & Tipton 2006). However, the results of reliable numerical simulations (Kokkinakis *et al.* 2015) show that the profile of $\tilde{K}_f$ does deviate from the parabolic profile. To match the RANS profiles with physical profiles, researchers have to adjust the model coefficients again (Kokkinakis *et al.* 2015). However, Dimonte and Tipton's method failed in guiding the adjustment of the model coefficients in such a situation. We think that the failure of Dimonte and Tipton's method in predicting the statistical profiles is essentially attributed to the non-physical assumption about the specific form of $\boldsymbol{F}_{RANS}$, i.e. $\bar{\boldsymbol{F}}_{apri}$. However, we find it is difficult to simply extend this method because a strict analytical solution of the RANS equation (node 3), and, thus, a set of model coefficients (node 4), can be obtained if and only if the specific $\boldsymbol{F}_{RANS}$ assumed by Dimonte & Tipton (2006) (node 2) is used.

In this paper, based on Dimonte and Tipton's work, we propose an approximate method to determine a set of model coefficients that can reproduce the physical evolution in both temporal scalings and spatial profiles. Although the idea is similar to that of Dimonte and Tipton's work, as shown by the solid arrows (nodes 1–7) in figure 1, it is

necessary to re-emphasize the overall logic as follows. Firstly, for a basic mixing problem, the corresponding physical evolution $\boldsymbol{F}_{phy}$ (node 1) is actually known (see § 2.1). Secondly, the goal of RANS simulation is to produce $\boldsymbol{F}_{RANS} \to \boldsymbol{F}_{phy}$ (node 7). Therefore, the ideal RANS solution (node 6) is actually deterministic. Next, it is natural to ask the question: given the deterministic RANS model (node 5) and RANS evolution $\boldsymbol{F}_{RANS}$ (node 6), what kind of model coefficients (node 4) should be set in the RANS model to produce such a solution?

The above question is trivial but its answer is non-trivial. In this paper we put forward a new method to try to answer this question. In this method, in contrast to the traditional method of forward solving $\boldsymbol{F}_{RANS}$ (from node I to node IV), we inversely solve the model coefficients by giving $\boldsymbol{F}_{RANS}$ (from node 1 to node 4), as shown in figure 1. The thinking is trivial, but the realisation of such a thinking needs a new idea, which will be presented in the next paragraph. This method is first applied to the basic 1-D incompressible problems with $R \to 1$. For these simple problems, we can derive a set of algebraic constraint relations, from which many sets of possible model coefficients can be obtained. Here, during this derivation, we specifically leave one degree of freedom with below consideration. In practical applications, problems generally involve unsteady and widely varied R. Therefore, the model coefficients should work not only for problems with $R \to 1$ but also for arbitrary R. The remaining degree of freedom is just used to meet the additional requirement. Considering this additional requirement, a unique set of model coefficients is determined.

This new method or idea is inspired by the famous Reynolds decomposition. In 1895 Reynolds proposed the well-known Reynolds decomposition to study turbulence, i.e.

$$f = \bar{f} + f', \tag{3.1}$$

where f denotes a fluctuating signal of an arbitrary physical quantity in a turbulence field, $\bar{f}$ is the corresponding statistical signal averaged along either temporal, spatial or ensemble directions, and its deviation from f is defined as fluctuation f'. Now, we will introduce an idea similar to the Reynolds decomposition to determine the values of the model coefficients. Noting that (i) on the one hand, it is nearly impossible to formulate RANS solution $\boldsymbol{F}_{RANS}$ exactly in advance, and (ii) on the other hand, a satisfactory RANS solution should approximately capture the physical evolution (i.e. $\boldsymbol{F}_{RANS} \approx \boldsymbol{F}_{phy}$), we thus define a decomposition similar to Reynolds decomposition as

$$\boldsymbol{F}_{RANS} \equiv \bar{\boldsymbol{F}}_{apri} + \boldsymbol{F}', \tag{3.2}$$

where $\bar{\boldsymbol{F}}_{apri}$ is an *a priori* analytical evolution set by referring to the physical evolution of the classical 1-D mixing problem as $\bar{\boldsymbol{F}}_{apri} \approx \boldsymbol{F}_{phy}$, and its deviation from $\boldsymbol{F}_{RANS}$ is a high-order small quantity $\boldsymbol{F}'$. The substitution of this decomposition into a symbolised RANS equation gives

$$\partial \boldsymbol{G}(\bar{\boldsymbol{F}}_{apri} + \boldsymbol{F}') = \boldsymbol{0}. \tag{3.3}$$

It is nearly impossible to give an analytical $\bar{\boldsymbol{F}}_{apri}$ that accurately equals $\boldsymbol{F}_{RANS}$; so, either $\boldsymbol{F}'$, or equivalently $\partial \boldsymbol{G}(\bar{\boldsymbol{F}}_{apri})$, would not equal zero at arbitrary spatial position x. Interestingly, at any given time t, integrating (3.3) along the mixing evolution direction x

would yield

$$\int \partial \boldsymbol{G}(\bar{\boldsymbol{F}}_{apri} + \boldsymbol{F}')\,\mathrm{d}x = \partial \boldsymbol{G}\left(\int \bar{\boldsymbol{F}}_{apri}\,\mathrm{d}x + \int \boldsymbol{F}'\,\mathrm{d}x\right) = \boldsymbol{0}, \tag{3.4}$$

where the order of integrals and differentials is exchanged. For this integration form, as long as the profile of $\bar{\boldsymbol{F}}_{apri}$ is assumed closely enough to that of $\boldsymbol{F}_{RANS}$, $\int \boldsymbol{F}'\,\mathrm{d}x$ would be much smaller than $\int \bar{\boldsymbol{F}}_{apri}\,\mathrm{d}x$ and, thus, can be neglected to give an approximation as

$$\int \partial \boldsymbol{G}(\bar{\boldsymbol{F}}_{apri})\,\mathrm{d}x \approx \boldsymbol{0}. \tag{3.5}$$

As will be demonstrated later, the approximated integration relation of (3.5) is crucial in establishing algebraic relations among model coefficients.

Now for a fully developed 1-D turbulent mixing, as discussed in § 2.1, its physical profiles evolve self-similarly. The *a priori* analytical solution of the RANS equation, $\bar{\boldsymbol{F}}_{apri}$, can thus be approximately formulated in a separated temporal–spatial variable form by referring to (2.7) to give

$$\bar{\boldsymbol{F}}_{apri}(x, t, C_A, \ldots, N_L) \approx \boldsymbol{F}_{phy} = \boldsymbol{F}_{ref} + \boldsymbol{F}(t, C_A, \ldots, N_L)\boldsymbol{F}(x_{non\text{-}dim}, C_A, \ldots, N_L). \tag{3.6}$$

Based on this form, substituting (3.6) into (3.5) would yield many algebraic relations among model coefficients. Firstly, algebraic constraint relations among model coefficients can be obtained directly by considering the independence of temporal evolution on the spatial variable. Secondly, the integration would eliminate the spatial variable x, further producing additional algebraic constraint relations among model coefficients. Consequently, the values of model coefficients can be obtained by solving all the algebraic constraint relations jointly.

Following the above logic, the model coefficients determined with the new method can produce $\boldsymbol{F}_{RANS}$ exactly equalling $\bar{\boldsymbol{F}}_{apri}$ if and only if the preset $\bar{\boldsymbol{F}}_{apri}$ is just the exact RANS solution. This ideal situation cannot be achieved in practice. In practice, what we can do is just to preset an *a priori* evolution $\bar{\boldsymbol{F}}_{apri} \approx \boldsymbol{F}_{phy}$. Consequently, the corresponding coefficient obtained can only produce $\boldsymbol{F}_{RANS} \approx \boldsymbol{F}_{phy}$. To obtain a set of model coefficients producing $\boldsymbol{F}_{RANS} \to \boldsymbol{F}_{phy}$, we need to further slightly adjust some coefficients by fully using the algebraic constraint relations established in this paper, as demonstrated in § 4.1.

3.2. *Derivations for problems with quasi-unity density ratio*

Following the aforementioned logic, the closer the value of $\int \boldsymbol{F}'\,\mathrm{d}x$ approaches to zero, the more accurate the current method is. In other words, if the value of $\bar{\boldsymbol{F}}_{apri}$ is close to that of $\boldsymbol{F}_{RANS}$ then $\boldsymbol{F}_{RANS}$ is closer to $\boldsymbol{F}_{phy}$. Therefore, it is crucial to preset an *a priori* evolution $\bar{\boldsymbol{F}}_{apri}$. In this paper we preset $\bar{\boldsymbol{F}}_{apri}$ by referring to the physical evolution $\boldsymbol{F}_{phy}$ of 1-D R–T, R–M and K–H mixing problems. Specifically, similar to Dimonte & Tipton (2006), we preset $\bar{\boldsymbol{F}}_{apri}$ with the simplest 1-D incompressible mixing problem with $R \to 1$. In this section we only derivate the constraint relations among model coefficients for problems with $R \to 1$. The extension from $R \to 1$ to arbitrary R will be discussed in § 4.1.

As discussed in § 2.1, the evolution is self-similar when the turbulent mixing is fully developed. According to (2.7), to formulate the self-similar evolution, a length scale is needed. Obviously, the mixing width is a natural length scale. For problem with $R \to 1$,

considering the symmetry in the mixing width between the bubble mixing zone and the spike mixing zone, the half-width of the total mixing zone is used as the length scale in this paper, i.e. $\ell(t) = H(t)/2 = h(t)$. Using this length scale, two non-dimensional length scales are defined as

$$\chi(x,t) \equiv x/h(t), \quad X(x,t) \equiv 1 - \chi^2(x,t). \tag{3.7a,b}$$

Obviously, across the mixing zone and for the problem with $R \to 1$, the first definition yields a signed spatial coordinate $\chi \in [-1, 1]$, which can be used in formulating the physical quantity whose spatial profile is asymmetric about the interface, such as the mass fraction. In contrast, the second definition yields an unsigned spatial coordinate $X(x,t) \in [0, 1]$, which can be used in formulating the symmetrical physical quantity, e.g. turbulent kinetic energy.

By referring to the self-similar evolution of 1-D R–T, R–M and K–H mixing problems, we preset the $\bar{\boldsymbol{F}}_{apri}$ across the mixing zone with the aid of the above definitions as

$$\bar{\boldsymbol{F}}_{apri}(x) \equiv \begin{cases} \tilde{e}(x,t) = \tilde{e}_{ref} + \tilde{e}_0(t)X, \\ \tilde{h}(x,t) = \tilde{h}_{ref} + \tilde{h}_0(t)X, \\ \tilde{Y}_1(x,t) = 1/2 - \chi/2, \\ \tilde{K}_f(x,t) = \tilde{K}_{f0}(t)X^s, \\ \tilde{L}(x,t) = \tilde{L}_0(t)X^r, \\ \tilde{v}_{KH}(x,t) = (\tilde{v}_{low} + \tilde{v}_{high})/2 + \chi(\tilde{v}_{high} - \tilde{v}_{low})/2, \end{cases} \tag{3.8}$$

where the subscript 0 denotes the central position of the mixing zone. Equation (3.8) gives the analytical evolution, in the form of separated temporal and spatial variables, of inner energy $\tilde{e}$, enthalpy $\tilde{h}$, mass fraction $\tilde{Y}_1$, turbulent kinetic energy $\tilde{K}_f$ and turbulent eddy scale $\tilde{L}$, respectively. In particular, the K–H mixing problem is two-dimensional in essence, and we also formulate the additional velocity parallel to the unperturbed interface $\tilde{v}_{KH}$ (only for K–H mixing problems) with the velocity of low-speed fluid $\tilde{v}_{low}$ and the velocity of high-speed fluid $\tilde{v}_{high}$.

Similar to Dimonte and Tipton's work, the variation of $\tilde{v}$, $\tilde{e}$, $\tilde{h}$ and $\tilde{Y}_1$ with spatial coordinator χ is approximated simply with a linear function. Obviously, this approximation would lead to a sharp transition from the mixed zone to the unmixed zone. In fact, this transition is smooth in physics, and a formulation with a heaviside-like function is more reasonable. However, the use of a linear function not only makes analytical solutions possible but also can drastically simplify the operations. Therefore, this approximation is preserved, and the deviation of smooth transition from sharp transition is further considered through slight adjustments of some parameters (i.e. the shape parameter shown in § 4.1). As for the evolution of turbulent kinetic energy $\tilde{K}_f$ and turbulent eddy scale $\tilde{L}$, their variations are approximated with a power law function of symmetrical spatial coordinators, i.e. X^s and X^r. In Dimonte & Tipton (2006), to analytically solve the RANS equation, the values of r and s are specified as $r = 1/2$ and $s = 1$. However, the implicit LES results (Youngs 2013; Kokkinakis *et al.* 2015) imply that this approximation actually deviates from the physical evolution. We think it is this unphysical approximation that leads to the failure of Dimonte and Tipton's method in predicting the spatial profiles. To avoid this unphysical assumption, in this paper we do

not limit the values of real r and s. Moreover, all the profiles are formulated with the form of separated variables. The terms explicitly include a time variable quantifying the evolution of amplitude at the interface 0, while the terms explicitly include spatial variables quantifying the shape of the spatial profiles. Finally, in physics the evolution of the length scale of the characteristic eddy $\tilde{L}_0(t)$ closely relates to the mixing width $h(t)$. To connect the two quantities, we introduce a non-dimensional $\beta(t)$ to quantify their ratio, and due to the self-similarity, this ratio is further assumed as a steady constant, i.e.

$$\beta(t) \equiv \tilde{L}_0(t)/h(t) \approx const. \tag{3.9}$$

As discussed in § 3.1, the values of model coefficients are determined by imposing the $\bar{\boldsymbol{F}}_{apri}$ into the RANS equation. For the 1-D incompressible mixing problem with $R \to 1$, the general RANS equation can be simplified as

$$\mathrm{D}\tilde{e}/\mathrm{D}t = D_E - \sqrt{2\tilde{K}_f}[C_B A_L(x) g - 2C_D \tilde{K}_f/\tilde{L}], \tag{3.10}$$

$$\mathrm{D}\tilde{Y}_1/\mathrm{D}t = \partial_x[C_\mu \tilde{L}\sqrt{2\tilde{K}_f}/N_Y(\partial_x \tilde{Y}_1)], \tag{3.11}$$

$$\mathrm{D}\tilde{K}_f/\mathrm{D}t = \partial_x[C_\mu \tilde{L}\sqrt{2\tilde{K}_f}/N_k(\partial_x \tilde{K}_f)] + \underbrace{C_\mu \tilde{L}\sqrt{2\tilde{K}_f}(\partial_x \tilde{v})^2}_{only\ K-H} + \sqrt{2\tilde{K}_f}[\underbrace{C_B A_L(x) g}_{only\ R-T} - C_D 2\tilde{K}_f/\tilde{L}], \tag{3.12}$$

$$\mathrm{D}\tilde{L}/\mathrm{D}t = \partial_x[C_\mu \tilde{L}\sqrt{2\tilde{K}_f}/N_L(\partial_x \tilde{L})] + C_L\sqrt{2\tilde{K}_f}, \tag{3.13}$$

where $D_E = \partial_x[C_\mu \tilde{L}\sqrt{2\tilde{K}_f}/N_e(\partial_x \tilde{e})]$ or $D_E = \partial_x[C_\mu \tilde{L}\sqrt{2\tilde{K}_f}/N_h(\partial_x \tilde{h})]$ in different papers, $A_L(x) \equiv [C_A \tilde{L}(x)/\bar{\rho}]\partial_x \bar{\rho}$ is x-dependent local Atwood number, $\mathrm{D}f/\mathrm{D}t \equiv \partial_t(\bar{\rho}f) + \nabla \cdot (\bar{\rho}\tilde{\boldsymbol{u}}f)$ is material derivation and the terms $C_\mu \tilde{L}\sqrt{2\tilde{K}_f}(\partial_x \tilde{v})^2$ and $C_B A_L(x) g$ are involved only for K–H and R–T problems, respectively. Equation (3.10) is derived by subtracting the turbulent kinetic energy equation (1.5) and mean kinetic energy equation from the total energy equation (1.3), and the mean kinetic energy equation can be obtained through a dot product operation between the momentum equation (1.2) and velocity.

Before further derivations, we first introduce the following differential relations to simplify the derivations:

$$\dot{\tilde{L}}_0(t)/\tilde{L}_0(t) = \dot{h}(t)/h(t), \tag{3.14}$$

$$\mathrm{D}f/\mathrm{D}t = f_0(t) q X^{q-1}(x,t) 2\chi^2 \dot{\tilde{L}}_0(t)/\tilde{L}_0(t) + X^q(x,t)\dot{f}_0(t), \tag{3.15}$$

$$f(x,t) \equiv f_{const} + f_0(t) X^q(x,t), \tag{3.16}$$

$$\partial_x(X^q) = q X^{q-1}\partial_x X = 2\chi q X^{q-1}/h(t), \tag{3.17}$$

$$\partial_x[X^l \partial_x(X^q)] = \partial_x[-2\chi q X^{q+l-1}/h(t)] = 2q[2(q+l-1)\chi^2 X^{q+l-2} - X^{q+l-1}]/h^2(t). \tag{3.18}$$

Here both q and l are real, f_{const} is a constant and $\dot{f}$ denotes a derivation to time. Equation (3.14) is derived from (3.9). In addition, we also introduce the integral relations

$$f_1(r) \equiv \int_0^1 X^{(r-1)}\,\mathrm{d}\chi \approx 1.1/(r+0.3)+0.16, \tag{3.19}$$

$$f_2(r) \equiv \int_0^1 X^{r}\,\mathrm{d}\chi \approx 0.935/(r+1.25)+0.25, \tag{3.20}$$

$$f_3(r) \equiv \int_0^1 X^{1-r}\,\mathrm{d}\chi \approx -0.92/(r-2.25)+0.26, \tag{3.21}$$

$$f_4(r) \equiv \int_0^1 X^{2(1-r)}\,\mathrm{d}\chi \approx -0.52/(r-5/3)+0.22, \tag{3.22}$$

$$f_5(r) \equiv \int_0^1 X\,\mathrm{d}\chi = 2/3, \tag{3.23}$$

$$f_6(r) \equiv \int_0^1 X^{3-4r}\,\mathrm{d}\chi \approx -0.25/(r-1.07)+0.22, \tag{3.24}$$

where the real number $r \in (0, 1)$. It is worth pointing out that the expression of $f_5(r)$ is different from the form of our earlier work by Xiao *et al.* (2020), where $f_5(r) \equiv \int_0^1 X^{1-2r}\,\mathrm{d}\chi \approx -0.447/(r-1.11)+0.26$ was used and its value approximates to 0.75 when $r = 0.2$. This is because the new expression (3.23) is under more rigorous derivation, as shown later by (3.43)–(3.48). However, this change is proven to have marginal influence on the final results of the previous work (Xiao *et al.* 2020). Except for the (3.23), other integrals cannot be expressed with elementary functions. Therefore, they are first calculated numerically and then fitted with the inverse proportion function of the second expression, as shown in figure 2.

Now we begin to determine the values of model coefficients. We begin from the model coefficients that did not appear in (3.10)–(3.13), i.e. C_P and C_C. Different from the original K–L model (Dimonte & Tipton 2006), to describe the K–H shear mixing problem, the classical eddy viscosity hypothesis is used in the current model. To model the Reynolds stress with an equal trace, the following classical constant C_P is used:

$$C_P = 2/3. \tag{3.25}$$

As for C_C, due to the incompressible constraint, it vanishes in (3.13) from (1.6). In (1.6) the term $C_C\bar{\rho}\tilde{L}\boldsymbol{\nabla}\cdot\tilde{\boldsymbol{u}}$ describes compression effects. Following Dimonte & Tipton (2006) we determine C_C by assuming that the total mass in the eddies $\propto \bar{\rho}\tilde{L}^3$ is conserved under compression, namely,

$$\mathrm{D}(\bar{\rho}\tilde{L}^3)/\mathrm{D}t = 3\tilde{L}^2\bar{\rho}(\mathrm{D}\tilde{L}/\mathrm{D}t) + \tilde{L}^3(\mathrm{D}\bar{\rho}/\mathrm{D}t) = 0. \tag{3.26}$$

Substituting the continuity equation of $\mathrm{D}\bar{\rho}/\mathrm{D}t = -\bar{\rho}\boldsymbol{\nabla}\cdot\tilde{\boldsymbol{u}}$ into (3.26) gives

$$\bar{\rho}(\mathrm{D}\tilde{L}/\mathrm{D}t) = \bar{\rho}\tilde{L}\boldsymbol{\nabla}\cdot\tilde{\boldsymbol{u}}/3. \tag{3.27}$$

Comparing this relation with (1.6) implies that

$$C_C = 1/3. \tag{3.28}$$

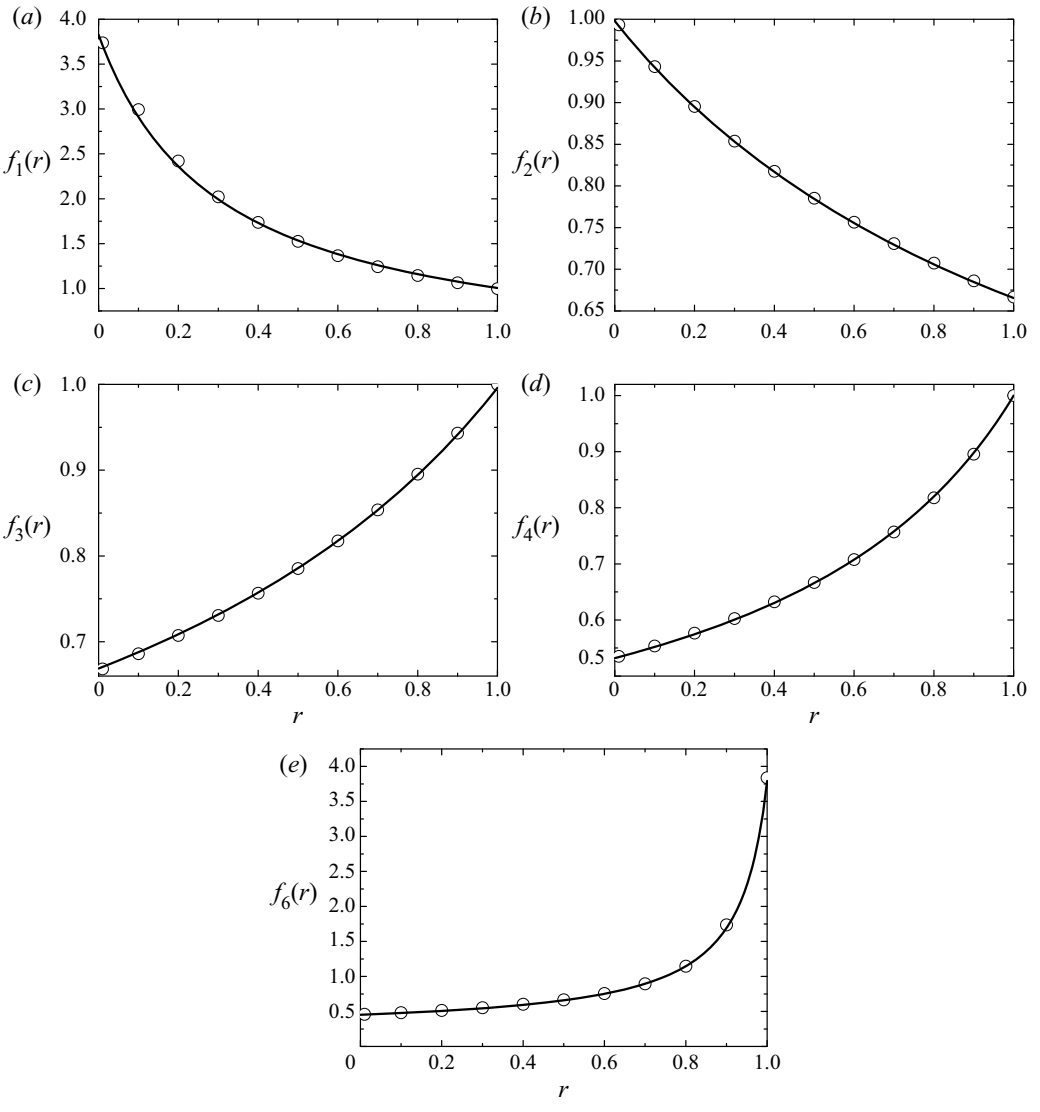

FIGURE 2. The variations of newly defined integrals $f_{1,2,3,4,6}(r)$, as shown in (3.19)–(3.22), (3.24) with power index r. The symbols give the variations by numerically integrating (3.19)–(3.22), (3.24). The lines plot the variations with fitted function, as shown on the right-hand side of (3.19)–(3.22), (3.24). The comparisons show that the fitted functions agree very well with numerical integrals in the range of $r \in (0, 1)$.

As mentioned above, the mixing model is driven by the production term of the turbulent kinetic energy equation. Specifically, for the K–L model and (3.12), the production term $C_B A_L(x)g$ is established from the buoyancy term of the buoyancy-drag model (Dimonte 2000; Zhang *et al.* 2016), which is very successful in predicting the evolution of mixing width, the most important quantity. Naturally, the mixing width predicted by the K–L model is also determined dominantly by the buoyancy term $C_B A_L(x)g$, with the strongest driving source located at the centre of mixing zone, i.e. $C_B A_L(0)g$. Therefore, to ensure that the mixing width predicted by the K–L model is comparable to that by the

buoyancy-drag model, we require that $C_B A_L(0)g$ has the same level as the source term of buoyancy-drag model $C_B Ag$. In other words, $A_L(0) \sim A$. From the definition of $A_L(x)$, $\tilde{L}(x,t)$ and β, we can derive the following relations with one-order difference:

$$A_L(x) \approx \frac{C_A \tilde{L}_0(t)}{\bar{\rho}} \frac{\rho_h - \rho_l}{2h(t)} X^r \approx \frac{C_A \tilde{L}_0(t)}{h(t)} \frac{\rho_h - \rho_l}{\rho_h + \rho_l} X^r \approx C_A \beta A X^r. \tag{3.29}$$

Here the approximation $\bar{\rho} \approx (\rho_h + \rho_l)/2$ is used. Obviously, to meet the requirement of $A_L(0) \sim A$, we need to set

$$C_A = 1/\beta. \tag{3.30}$$

For the species equation, substituting (3.8) into (3.11) and using the relations of (3.14)–(3.18) yield

$$N_Y \dot{\tilde{L}}_0 / [C_\mu \beta^2 (2r + s) \sqrt{2\tilde{K}_{f0}}] = X^{r+s/2-1}. \tag{3.31}$$

Noting that the left-hand and right-hand sides of (3.31) depend only on time and spatial coordinates, respectively, the equality exists if and only if $r + s/2 - 1 = 0$. Thus, we have

$$r = 1 - s/2, \tag{3.32}$$

$$N_Y \dot{\tilde{L}}_0 = 2C_\mu \beta^2 \sqrt{2\tilde{K}_{f0}}. \tag{3.33}$$

In physics the positive turbulent kinetic energy and length scale of eddy imply that the power index r and s in (3.8) should be larger than zero. Equation (3.32) further implies that $r \in (0, 1)$. From the above derivation we can find the constraint on the power index r and s of the profiles of turbulent kinetic energy and length scale of eddy, i.e. (3.32), essentially comes from the *a priori* approximation that the profile of mass fraction varies linearly with spatial coordinate χ.

Similar to the above operations for species equation, we further substitute (3.8) into the equation of turbulent eddy scale, i.e. (3.13). After some complex operations with the aid of (3.14)–(3.18), we finally obtain

$$\begin{aligned}&[\dot{\tilde{L}}_0(t) - 2rC_\mu \beta^2 \sqrt{2\tilde{K}_{f0}}/N_L] 2r(1 - X) X^{r-1} + [\dot{\tilde{L}}_0(t) + 2rC_\mu \beta^2 \sqrt{2\tilde{K}_{f0}}/N_L] X^r \\ &\quad = C_L \sqrt{2\tilde{K}_{f0}} X^{(1-r)}.\end{aligned} \tag{3.34}$$

Furthermore, to simplify the expressions, we define non-dimensional φ_1 and φ_2 as

$$\varphi_1(r) \equiv 2C_\mu \beta^2 / (C_L N_L), \tag{3.35}$$

$$\varphi_2(r) \equiv 2\dot{\tilde{L}}_0(t) / (C_L \sqrt{2\tilde{K}_{f0}}), \tag{3.36}$$

where both φ_1 and φ_2 implicitly depend on the power index r. With these definitions, (3.33) becomes

$$N_Y = 2N_L \varphi_1(r) / \varphi_2(r). \tag{3.37}$$

More importantly, (3.34) can be rearranged to give

$$\begin{aligned}F_L[X(\chi), r] \equiv\ &[\varphi_2(r) - 2r\varphi_1(r)] r(1 - X) X^{r-1} + [\varphi_2(r)/2 \\ &+ \varphi_1(r) r] X^r - X^{(1-r)} = 0.\end{aligned} \tag{3.38}$$

It can be easily verified that $F_L[X(\chi), r] \equiv 0$ by giving $\varphi_1(r) = \varphi_2(r) = 1$ and $r = 1/2$, which is the special solution given by Dimonte & Tipton (2006). However, as we

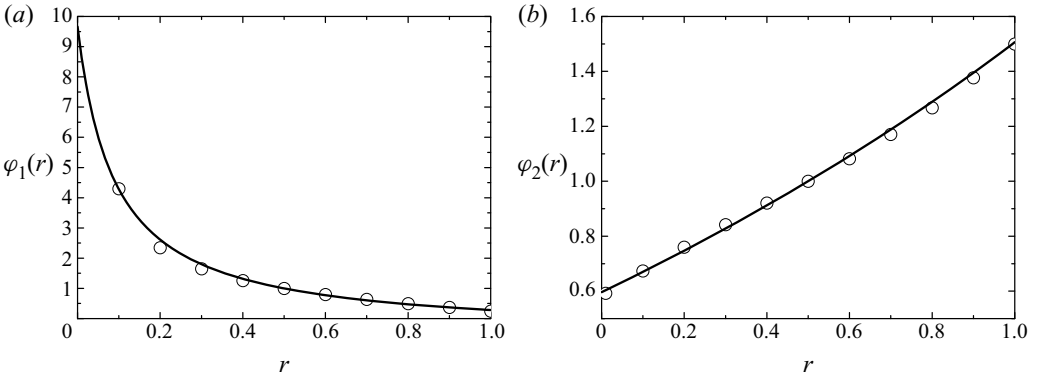

FIGURE 3. The variations of newly defined integrals $\varphi_{1,2}(r)$ (as shown in (3.41) and (3.42)) with power index r. The symbols give the variations by numerically integrating (3.41) and (3.42). The lines plot the variations with fitted function, as shown on the right-hand side of (3.41) and (3.42). The comparisons show that the fitted functions agree very well with numerical integrals in the range of $r \in (0, 1)$.

mentioned above, a shortcoming of Dimonte and Tipton's special solution is that the corresponding model coefficients obtained could not reproduce the physical profiles. In this paper we devote to finding an approximate solution for arbitrary r and s. To achieve this goal, based on the logic presented in § 3.1, we turn to require that the integral of $F_L[X(\chi), r]$ across the mixing zone approximates zero. Furthermore, considering that (3.38) involves both $\varphi_1(r)$ and $\varphi_2(r)$, we implement the integral for both X and χ to uniquely determine the values of $\varphi_1(r)$ and $\varphi_2(r)$, i.e.

$$\int_0^1 F_L[X(\chi), r]\,\mathrm{d}\chi = 0, \tag{3.39}$$

$$\int_1^0 F_L[X(\chi), r]\,\mathrm{d}X = 0, \tag{3.40}$$

where, due to the symmetry, the non-dimensional integral interval is from 0 to 1. Substituting the definition of $F_L[X(\chi), r]$ given in (3.38) into (3.39) and (3.40), we can finally obtain the following relations after some complex operations:

$$\varphi_2(r) = \frac{G_3(r)G_4(r) - f_3(r)G_1(r)}{G_2(r)G_4(r) - G_5(r)G_1(r)} \approx -17.8/(r - 4.95) - 3, \tag{3.41}$$

$$\varphi_1(r) = \frac{G_3(r)}{G_1(r)} - \varphi_2\frac{G_2(r)}{G_1(r)} \approx 0.92/(r + 0.09) - 0.56. \tag{3.42}$$

Here $G_1(r) \equiv 2r - (2r^2 + r)/(r + 1)$, $G_2(r) \equiv (r - 1/2)/(r + 1) - 1$, $G_3(r) \equiv 1/(r - 2)$, $G_4(r) \equiv (2r^2 + r)f_2(r) - 2r^2 f_1(r)$ and $G_5(r) \equiv rf_1(r) + (1/2 - r)f_2(r)$. Similar to $f_i(r)$, (3.41) and (3.42) show that both $\varphi_1(r)$ and $\varphi_2(r)$ cannot be expressed with elementary functions, and we also use the inverse proportion function to fit their numerical integrals, as shown in figure 3. From figure 3 we can find that the current method successfully reproduces Dimonte and Tipton's results of $\varphi_1(r) = \varphi_2(r) = 1$ at $r = 1/2$.

Similarly, with the aid of (3.9), (3.14)–(3.18), (3.32), (3.35) and (3.36), we can also derive the following evolution equation for $\tilde{K}_f$ by substituting (3.8) into (3.12):

$$\begin{aligned}&\left[\frac{\varphi_2(r)}{4}-\frac{(1-r)N_L\varphi_1(r)}{N_k}\right]4(1-r)(1-X)X^{1-2r}\\&\quad+\left[\frac{1}{C_L}\frac{\tilde{L}_0(t)}{(2\tilde{K}_{f0})}\frac{\dot{\tilde{K}}_{f0}}{\sqrt{2\tilde{K}_{f0}}}+\frac{(1-r)N_L\varphi_1(r)}{N_k}\right]X^{2(1-r)}\\&=-\frac{C_D}{C_L}X^{3-4r}+\underbrace{\frac{C_\mu\beta^2}{4C_L}\frac{(\Delta\tilde{v})^2}{2\tilde{K}_{f0}}X}_{only\ K-H}+\underbrace{\frac{1}{C_L}\frac{\tilde{L}_0(t)}{(2\tilde{K}_{f0})}C_BA_0gX}_{only\ R-T},\end{aligned}\tag{3.43}$$

where the last two terms exist only for K–H and R–T mixing problems, respectively. Equation (3.43) is too complex to derive a general constraint among model coefficients. Here, we search for a possibly additional constraint with the principle that this constraint can minimise the complicity of (3.43). We find that the following constraint can greatly simplify (3.43):

$$\varphi_2(r)/4=\varphi_1(r)(1-r)N_L/N_k.\tag{3.44}$$

Under the constraint of (3.44), (3.43) becomes

$$\begin{aligned}\left[\frac{1}{C_L}\frac{\tilde{L}_0(t)}{(2\tilde{K}_{f0})}\frac{\dot{\tilde{K}}_{f0}}{\sqrt{2\tilde{K}_{f0}}}+\frac{\varphi_2(r)}{4}\right]X^{2(1-r)}&=-\frac{C_D}{C_L}X^{3-4r}+\underbrace{\frac{C_\mu\beta^2}{4C_L}\frac{(\Delta\tilde{v})^2}{2\tilde{K}_{f0}}X}_{only\ K-H}\\&\quad+\frac{1}{C_L}\frac{\tilde{L}_0(t)}{(2\tilde{K}_{f0})}C_BAgX.\end{aligned}\tag{3.45}$$

Later, we will use (3.45) to derivate other constraint relations of the model coefficients.

A further analytical operation of (3.45) is possible if $r=1/2$, as demonstrated by Dimonte & Tipton (2006). For arbitrary real r, however, an analytical operation is nearly impossible. To derive the constraint relations among model coefficients, we rethink the problem from two opposite perspectives. From a forward viewpoint, we are looking for such a set of model coefficients to reproduce the physical evolution of either R–T, R–M or K–H mixing problems. From a converse viewpoint, the physical evolution of R–T, R–M and K–H mixing problems should also meet (3.45). Therefore, the constraint relations among model coefficients can be approximately established by imposing the physical evolution law into (3.45), and not directly solve the equation. Next, this idea will be used for K–H, R–M and R–T mixing problems.

Firstly, for the K–H mixing problem, the growth of the total mixing width is given in (2.5). Combining (2.5), (3.9) and (3.36) and the relation of $H(t)=2h(t)$, we can derive

$$\tilde{K}_{f0}=[\beta\alpha_{KH}\Delta\tilde{v}/(\varphi_2C_L)]^2/2.\tag{3.46}$$

With the aid of (3.46), (3.45) can be simplified to

$$\begin{aligned}F_K^{KH}[X(\chi),r]&\equiv\varphi_2(r)X^{2(1-r)}/4-C_\mu C_L(\varphi_2/\alpha_{KH})^2X/4+X^{3-4r}C_D/C_L\\&=0.\end{aligned}\tag{3.47}$$

Using the same idea adopted in $\tilde{L}$, we can derive an approximate constraint relation with the weak constraint of $\int_0^1 F_K^{KH}[X(\chi), r]\,\mathrm{d}\chi = 0$ as

$$C_\mu = \frac{\varphi_2(r)f_4(r) + 4f_6(r)C_D/C_L}{C_L f_5(r)[\varphi_2(r)/\alpha_{KH}]^2}. \tag{3.48}$$

Secondly, for the classical R–M mixing problem with impulsive $g \approx 0$, the growth of the mixing width is given in (2.6). Combining (2.6), (3.9) and (3.36), we can derive that

$$\frac{1}{C_L}\frac{\tilde{L}_0(t)}{(2\tilde{K}_{f0})}\frac{\dot{\tilde{K}}_{f0}}{\sqrt{2\tilde{K}_{f0}}} = \frac{\varphi_2\tilde{L}_0\ddot{\tilde{L}}_0}{2\dot{\tilde{L}}_0^2} = \frac{\varphi_2}{2}\frac{\theta-1}{\theta}. \tag{3.49}$$

With the aid of (3.49), (3.45) can be simplified into

$$F_K^{RM}[X(\chi), r] \equiv \left[\varphi_2(r)(\theta-1)/(2\theta) + \varphi_2(r)/4\right]X^{2(1-r)} + X^{3-4r}C_D/C_L = 0. \tag{3.50}$$

Using the same idea adopted in $\tilde{L}$, we can derive an approximate constraint relation with the weak constraint of $\int_0^1 F_K^{RM}[X(\chi), r]\,\mathrm{d}\chi = 0$ as

$$C_L = \frac{C_D}{(2\theta)^{-1} - 3/4}\frac{f_6(r)}{\varphi_2(r)f_4(r)}. \tag{3.51}$$

Thirdly, for the classical R–T mixing problem with constant g, the growth of the mixing width is given in (2.4). Combining (2.4), (3.9) and (3.36), we can derive that

$$\frac{\tilde{L}_0}{2\tilde{K}_{f0}} = \frac{(C_L\varphi_2)^2}{16\beta\alpha_b Ag}, \tag{3.52}$$

$$\frac{\dot{\tilde{K}}_{f0}}{\sqrt{2\tilde{K}_{f0}}} = \frac{C_L\varphi_2}{4}\frac{2\tilde{K}_{f0}}{\tilde{L}_0}. \tag{3.53}$$

With the aid of (3.52) and (3.53), (3.45) can be simplified into

$$F_K^{RT}[X(\chi), r] \equiv \frac{\varphi_2(r)}{2}X^{2(1-r)} - \frac{C_B}{C_L}\left(\frac{C_L\varphi_2}{4}\right)^2\frac{1}{\beta\alpha_b}X + \frac{C_D}{C_L}X^{3-4r} = 0. \tag{3.54}$$

Using the same idea adopted in $\tilde{L}$, we can derive an approximate constraint relation with the weak constraint of $\int_0^1 F_K^{RT}[X(\chi), r]\,\mathrm{d}\chi = 0$ as

$$C_B = \frac{24\alpha_b}{C_A C_L}\left[\frac{f_4(r)}{2\varphi_2(r)} + \frac{C_D}{C_L}\frac{f_6(r)}{\varphi_2^2(r)}\right]. \tag{3.55}$$

Furthermore, the increment of turbulent kinetic energy and decrement of potential energy are expressed as, respectively,

$$\Delta E_k = \int_{-h}^{h}\bar{\rho}\tilde{K}_f\,\mathrm{d}x = \int_{-h}^{h}\bar{\rho}(x)\tilde{K}_{f0}(t)[1-(x/h)^2]^{2(1-r)}\,\mathrm{d}x \approx (\rho_h+\rho_l)\tilde{K}_{f0}hf_4(r), \tag{3.56}$$

$$\Delta PE = \left(\int_{-h}^{0}\rho_l gx\,\mathrm{d}x + \int_0^h\rho_h gx\,\mathrm{d}x\right) - \left(\int_{-h}^{0}\bar{\rho}gx\,\mathrm{d}x + \int_0^h\bar{\rho}gx\,\mathrm{d}x\right) \approx \frac{\rho_h-\rho_l}{6}gh^2, \tag{3.57}$$

where the mean density $\bar{\rho}(x)$ is approximated as $\bar{\rho}(x) \approx ((\rho_h + \rho_l)/2) + ((\rho_h - \rho_l)/2h)x$. Using (2.4), (3.9) and (3.36), we can derive $\Delta E_k/\Delta PE = 48\alpha_b f_4(r)/[\varphi_2(r)C_A C_L]^2$, which gives

$$C_A = \frac{1}{C_L\varphi_2(r)}\sqrt{\frac{48\alpha_b f_4(r)}{(E_k/\Delta PE)}}. \tag{3.58}$$

Similar to the quadratic growth coefficient of the mixing width, we also define a quadratic growth coefficient of maximum turbulent kinetic energy α_K as $\alpha_K \equiv \tilde{K}_{f0}/(A_0 g t)^2$. Combining this definition and (2.4), (3.9) and (3.36) and (3.58), we can derive that

$$\alpha_K = \alpha_b \frac{(E_k/\Delta PE)}{6f_4(r)}, \tag{3.59}$$

which will be used in the next section to determine the final model coefficients.

Finally, with the aid of (3.9), (3.14)–(3.18), (3.32), (3.35) and (3.36) and assuming that γ is constant, we can also derive the following inner energy equation by substituting (3.8) into (3.10):

$$\frac{\varphi_2(r)C_L}{\tilde{L}_0(t)}\tilde{e}_0(t)(1-X) + \dot{\tilde{e}}_0(t)X = \Psi\frac{2\beta^2 C_\mu}{\tilde{L}_0(t)}[2(1-X) - X] - C_B AgX + C_D\frac{(2\tilde{K}_{f0})}{\tilde{L}_0(t)}X^{3-4r}. \tag{3.60}$$

Here, corresponding to different models (Kokkinakis *et al.* 2015), $\Psi = \gamma\tilde{e}_0/N_h$ or $\tilde{e}_0/N_e$. In principle, we can conduct similar operations for the turbulent kinetic energy equation to derive new constraint relations among model coefficients. However, considering that little knowledge is known for the evolution of inner-energy-associated quantities, we determine the coefficients of N_e or N_h with the following idea. The inner energy equation consistent with (3.10) is

$$(\bar{\rho}\tilde{e})_t + \partial_x[\tilde{u}(\bar{p} + \bar{\rho}\tilde{e})] = D_E - S_{k_f}. \tag{3.61}$$

For the incompressible limit with $\gamma =$ constant, we have $e = p/[\rho(\gamma - 1)]$, where $p \equiv p_0 + p'$, $p_0 \to \infty$ and $p_0 \gg p'$. The dominant terms of (3.61) at $A \to 0$ then gives

$$\partial_x\left(\frac{\gamma p_0}{\gamma - 1}u\right) = \partial_x\left[\frac{\mu_t}{N_e}\partial_x\left(\frac{p_0}{\gamma - 1}\frac{1}{\bar{\rho}}\right)\right] \quad \text{or} \quad \partial_x\left(\frac{\gamma p_0}{\gamma - 1}u\right) = \partial_x\left[\frac{\mu_t}{N_h}\partial_x\left(\frac{\gamma p_0}{\gamma - 1}\frac{1}{\bar{\rho}}\right)\right]. \tag{3.62a,b}$$

Consequently, we can obtain

$$\partial_x\left[u - \frac{\mu_t}{\gamma N_e}\partial_x\left(\frac{1}{\bar{\rho}}\right)\right] = 0 \quad \text{or} \quad \partial_x\left[u - \frac{\mu_t}{N_h}\partial_x\left(\frac{1}{\bar{\rho}}\right)\right] = 0. \tag{3.63a,b}$$

In addition, for the incompressible limit, the mass fraction (1.4) can be reduced to (see the detailed derivations in Livescu 2013) $\nabla \cdot (\tilde{\boldsymbol{u}} - (\mu_t/N_Y)\nabla(1/\bar{\rho})) = 0$, whose 1-D form

reads as

$$\partial_x \left[u - \frac{\mu_t}{N_Y} \partial_x \left(\frac{1}{\bar{\rho}} \right) \right] = 0. \tag{3.64}$$

Comparison of (3.64) and (3.63*a*,*b*) yields the constraint relations

$$N_e = N_Y/\gamma \quad \text{or} \quad N_h = N_Y, \tag{3.65a,b}$$

where the different constraint relations correspond to different models (Kokkinakis *et al.* 2015).

Equations (3.25), (3.28), (3.30), (3.32), (3.37), (3.41), (3.42), (3.44), (3.48), (3.51), (3.55), (3.58), (3.59) and (3.65*a*,*b*) involve 21 variables. These include one variable characterising the fluid property (i.e. γ), seven variables characterising mixing evolution (i.e. $\alpha_b, \alpha_{KH}, \theta, \Delta E_k/\Delta PE, s, r, \alpha_k$), two variables defined in this paper (i.e. φ_1, φ_2) and 11 variables of model coefficients $C_A, C_B, C_c, C_D, C_P, C_\mu, C_L, N_h(N_e)$, N_k, N_L, N_Y. Among the seven variables characterising mixing evolution, five variables of $\alpha_b, \alpha_{KH}, \theta, \Delta E_k/\Delta PE, s$ have clear physical meaning and can be easily measured in either numerical simulations or experiments. Therefore, the values of five variables are actually known, at least for experts working in this field. Furthermore, except for the known property parameter γ, the number of remaining variables to be determined are 15. The derived 14 algebraic relations, so there is only one degree of freedom. Consequently, given the value of any one undetermined variable, the others can be uniquely determined. Considering that (i) the drag coefficient C_D has a more clear physical meaning, and (ii) the value of C_D has been widely investigated in either buoyancy-drag model (Dimonte 2000; Zhang *et al.* 2016) or K–L model (Dimonte & Tipton 2006; Morgan & Greenough 2016), in this paper we leave the one degree of freedom to C_D.

Now given $\alpha_b, \alpha_{KH}, \theta, \Delta E_k/\Delta PE, s, \gamma$ and C_D, the final expressions to calculate the model coefficients are collected, in an order that each coefficient can be determined explicitly one by one, as

$$r = 1 - s/2, \tag{3.66}$$

$$C_c = 1/3, \tag{3.67}$$

$$C_p = 2/3, \tag{3.68}$$

$$C_L = \frac{C_D}{(2\theta)^{-1} - 3/4} \frac{f_6(r)}{\varphi_2(r) f_4(r)}, \tag{3.69}$$

$$C_A = \frac{1}{C_L \varphi_2(r)} \sqrt{\frac{48\alpha_b f_4(r)}{(\Delta E_k/\Delta PE)}}, \tag{3.70}$$

$$C_B = \frac{24\alpha_b}{C_A C_L} \left[\frac{f_4(r)}{2\varphi_2(r)} + \frac{C_D}{C_L} \frac{f_6(r)}{\varphi_2^2(r)} \right], \tag{3.71}$$

$$C_\mu = \frac{\varphi_2(r) f_4(r) + 4 f_6(r) C_D/C_L}{C_L f_5(r) (\varphi_2(r)/\alpha_{KH})^2}, \tag{3.72}$$

$$N_L = \frac{2C_\mu}{C_L C_A^2 \varphi_1(r)}, \tag{3.73}$$

$$N_k = N_L 4(1-r) \frac{\varphi_1(r)}{\varphi_2(r)}, \tag{3.74}$$

$$N_Y = 2N_L \frac{\varphi_1(r)}{\varphi_2(r)}, \tag{3.75}$$

$$N_e = N_Y/\gamma \quad \text{or} \quad N_h = N_Y, \tag{3.76a,b}$$

where $f_i(r)$ $(i = 1, \ldots\ldots, 6)$ and $\varphi_i(r)$ $(i = 1, 2)$ are given in (3.19)–(3.24) and (3.41)–(3.42), respectively.

Using (3.66)–(3.76*a*,*b*), it can be verified that Dimonte and Tipton's model coefficients can be recovered by giving $\alpha_b = 0.0625$, $\alpha_{KH} = 0.5$, $\theta = 0.25$, $\Delta E_k/\Delta PE = 0.5$, $s = 1$, $\gamma = 1.4$ and $C_D = 1.25$, thus validating the rationality of the current methodology indirectly. Moreover, giving $\alpha_b, \alpha_{KH}, \theta, \Delta E_k/\Delta PE, s, \gamma$ and C_D, we can always obtain a set of model coefficients with the current method. Solving the RANS equation with such a set of model coefficients would produce corresponding RANS evolution $\boldsymbol{F}_{RANS}$, from which we can measure another set of $\alpha_b, \alpha_{KH}, \theta, \Delta E_k/\Delta PE$ and s. A comparison of the two sets of $\alpha_b, \alpha_{KH}, \theta, \Delta E_k/\Delta PE$ and s can directly evaluate the approximation level of the current methodology. For the classical R–T, R–M and K–H mixing problems in § 2.2, the systematic RANS calculation for problems with $R \to 1$ and for different values of $\alpha_b, \alpha_{KH}, \theta, \Delta E_k/\Delta PE, s, \gamma$ and C_D are conducted with CFD^2 code. Without giving all the results, we summarize that although there exists a slight deviation between $\bar{\boldsymbol{F}}_{apri}$ and $\boldsymbol{F}_{RANS}$, the model coefficients obtained with the current methodology can always produce $\boldsymbol{F}_{RANS} \approx \boldsymbol{F}_{phy} \approx \bar{\boldsymbol{F}}_{apri}$. As an example, in figure 4 we demonstrate a specific result for the R–T test problem with $A = 0.1$. In this case, we set $\alpha_b = 0.05, \alpha_{KH} = 0.18$, $\theta = 0.25$, $\Delta E_k/\Delta PE = 0.5$, $s = 4/3$ and $\gamma = 1.4$ based on our understanding of mixing problems (see also § 2.1). The initial value of C_D is tentatively set as $1/(2\sqrt{2})$ by referring to Morgan & Greenough (2016). In figure 4 we can see that the RANS evolutions, either temporal or spatial scalings, are close to those preset evolutions, thus validating the current methodology. Moreover, as the above methodology is essentially an approximation theory, a slight deviation of $\boldsymbol{F}_{RANS}$ from $\bar{\boldsymbol{F}}_{apri}$ can be observed. However, the deviation has less influence on the determination of model coefficients and can be further improved by slightly adjusting a parameter shown in the next section.

4. Applications

4.1. *Procedures for determining coefficients (a specific example)*

In the previous section we document the derivations of the current theory and demonstrate that the model coefficients determined with the current method successfully produce $\bar{\boldsymbol{F}}_{apri} \approx \boldsymbol{F}_{RANS} \approx \boldsymbol{F}_{phy}$. However, before applying this method to practical applications, some problems still need to be solved. For problems with $R \to 1$, RANS simulation with model coefficients calculated from (3.66)–(3.76*a*,*b*) can produce $\boldsymbol{F}_{RANS} \approx \boldsymbol{F}_{phy} \approx \bar{\boldsymbol{F}}_{apri}$ if the desired evolution $\boldsymbol{F}_{phy}$ and a specific C_D are given. However, we have not shown how to determine the remaining degree of freedom of C_D. Consequently, for the same desired $\boldsymbol{F}_{phy}$, different sets of model coefficients can be obtained by different values of C_D. The following questions arise. (i) Among all the possible model coefficients for the problem with $R \to 1$, is there a set of model coefficients suitable for all R? (ii) Moreover, if the answer to the first question is yes then how does one find such a set of model coefficients with the aid of constraint relations (3.66)–(3.76*a*,*b*)? In this section, we will answer the two questions by applying the current method to a specific R–T mixing problem and demonstrate detailed procedures of determining model coefficients.

We try to answer the questions from the description of the evolution of mixing. As discussed in § 2.1, the mixing evolution can be described in three levels. In terms of

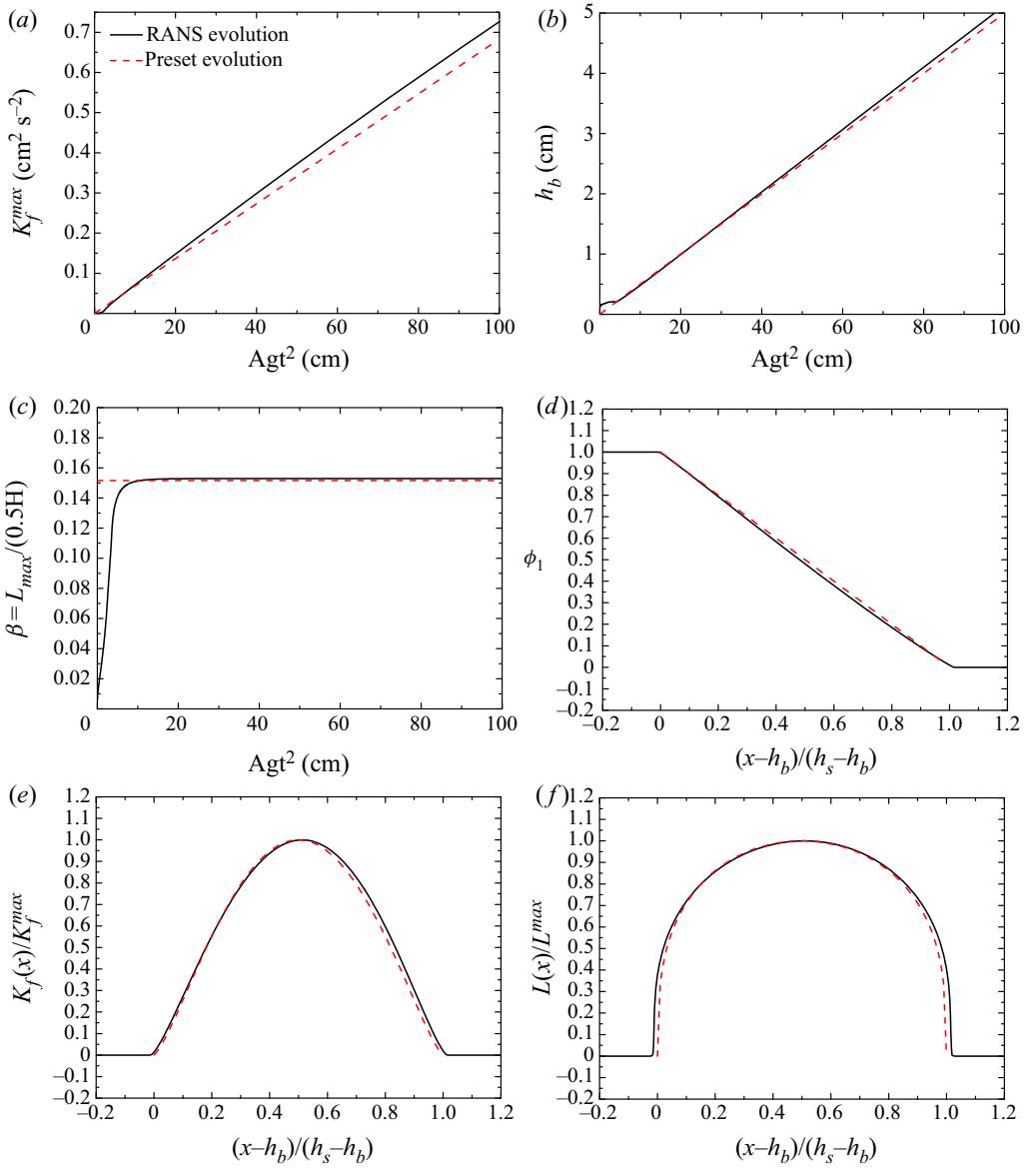

FIGURE 4. Comparison of the temporal evolutions (left) of (*a*) maximum turbulent kinetic energy $\tilde{K}_f^{max}$, (*b*) mixing width of bubble mixing zone h_b, and (*c*) self-similar parameter β versus Agt^2 and the spatial profiles (right) of (*d*) the volume fraction of a heavy fluid $\tilde{\phi}_1$, (*e*) re-normalised turbulent kinetic energy $\tilde{K}_f/\tilde{K}_f^{max}$ and (*f*) re-normalised length scale $\tilde{L}/\tilde{L}^{max}$ versus $(x-h_b)/(h_s-h_b)$ between RANS evolutions (solid lines) and preset evolutions (dashed lines). In this study the superscript *max* denotes the maximum value of quantity over the entire mixing zone at any given time. The RANS results of the R–T test problem with $A = 0.1$ are calculated with a set of model coefficients determined by $\alpha_b = 0.05$, $\alpha_{KH} = 0.18$, $\theta = 0.25$, $\Delta E_k/\Delta PE = 0.5$, $s = 4/3$, $\gamma = 1.4$ and $C_D = 1/(2\sqrt{2})$ (Morgan & Greenough 2016). The preset evolutions are given according to the current theory. Specifically, the preset evolutions of $\tilde{K}_f/\tilde{K}_f^{max}$, h_b and β are given theoretically by (3.59), (2.4) and both (3.30) and (3.70), respectively. The spatial profiles of ϕ_1, $\tilde{K}_f/\tilde{K}_f^{max}$ and $\tilde{L}/\tilde{L}^{max}$ are given by (3.8).

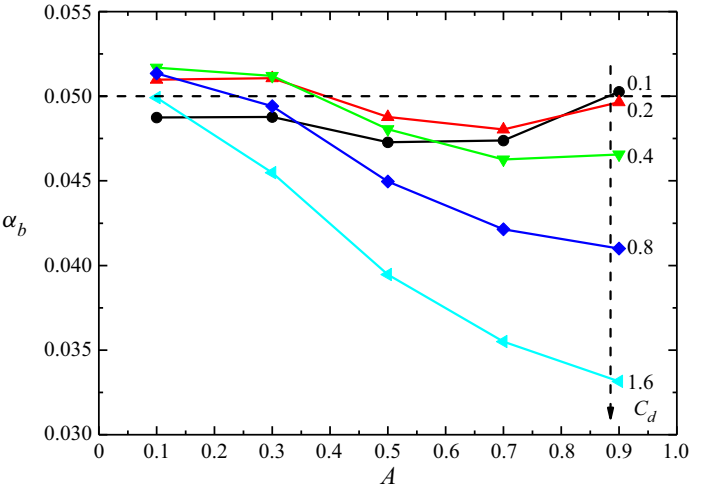

FIGURE 5. Variation of the measured α_b of RANS results with Atwood number A (or equivalent R) and model coefficient C_D. The RANS results are obtained with the model coefficients determined by providing $\alpha_b = 0.05$, $\alpha_{KH} = 0.18$, $\theta = 0.25$, $\Delta E_k/\Delta PE = 0.5$, $s = 4/3$, $\gamma = 1.4$ and different values of C_D. In this figure, α_b corresponding to five values of $C_D = 0.1$ (black line), 0.2 (red line), 0.4 (green line), 0.8 (blue line) and 1.6 (cyan line) is plotted. The values of α_b vary slightly with the methods used to calculate α_b. If the mixing width is assumed growing as $h_b = \alpha_b Ag(t + t_s)^2$, one can derive $h_b^{1/2} = \alpha_b^{1/2}\sqrt{Ag}(t + t_s)$, where t_s is the time origin of bubbles (Clark & Zhou 2003; Cabot & Cook 2006). In this situation, when plotting $h_b^{1/2}$ versus $\sqrt{Ag}t$, the asymptotic slope of the curve can be regarded as $\alpha_b^{1/2}$, and thus α_b. In contrast, if the mixing width is assumed growing as $h_b = \alpha_b Agt^2$, α_b is the asymptotic slope when plotting h_b versus Agt^2. The slight difference between the two methods has been discussed in Cabot & Cook (2006) and Zhou (2017*b*). In this figure α_b is measured using the latter method.

practical applications, the most important and fundamental level is the first level of the mixing width. If the mixing width is correctly captured, predicting higher levels (e.g. mixing profile) would not be too bad. Based on the analysis, we present the critical idea in determining the remaining degree of freedom of C_D, and, thus, the model coefficients, as follows: final C_D can be determined if its corresponding model coefficients can correctly predict the evolution of the mixing width at all density ratios. For the R–T mixing problem, the mixing width increases as shown in (2.4). Moreover, based on experiments (Read 1984; Youngs 1989; Dimonte & Schneider 2000) and numerical simulations (Zhou 2017*a*), researchers have identified that the quadratic grow coefficient α_b, equivalently to h_b, is nearly independent of density ratios, provided that the initial perturbations are similar (Dimonte 2004; Ramaprabhu *et al.* 2005; Banerjee & Andrews 2009; Olson & Jacobs 2009; Zhou 2017*b*).

Based on the above analysis, we determine the remaining degree of freedom, C_D, as per the following steps: (i) calculate model coefficients by providing the same values of α_b, α_{KH}, θ, $\Delta E_k/\Delta PE$, s and γ and different values of C_D; (ii) for different values of R, implement RANS simulations with the model coefficients obtained in step (i); (iii) measure α_b obtained from RANS results and plot the variations of α_b with R and C_D; (iv) select C_D that produces the R-independent α_b. In figure 5, after implementing the above procedures, we plot the variations of α_b with A and C_D. From this figure we can see that the value of α_b decreases monotonically as A when $C_D = 0.4$, 0.8 and 1.6, and

increases slightly as A when $C_D = 0.1$. Only when $C_D = 0.2$, α_b takes the constant value of 0.05 at all density ratios. Hence, the value of $C_D = 0.2$ is used hereafter.

With the aforementioned procedures, all the model coefficients can be determined, but the problem is not over. As mentioned in §§ 3.1 and 3.2, the model coefficients determined from (3.66)–(3.76*a*,*b*) can only produce $\boldsymbol{F}_{RANS} \approx \boldsymbol{F}_{phy}$ but cannot produce $\boldsymbol{F}_{RANS} \to \boldsymbol{F}_{phy}$, as the current method is essentially an approximation method. Specifically, in this method the profiles of $\tilde{\phi}_1$ and $\tilde{K}_f/\tilde{K}_f^{max}$ are preset as $(1-\chi)/2$ and X^s, respectively, and the corresponding RANS profiles are closest to the preset profiles (see figure 4). Consequently, a sharp transition nearby the outer edge of the mixing zone can be observed, slightly different from the smooth transition in experiments and numerical simulations (DNS or LES). Although a slight difference comes from approximations of the current method, it is possible to slightly adjust the model coefficients to produce profiles approaching physical results, based on the understanding of the current method. Next, we will address this problem.

To better quantify the shape of a profile, we have segmented a profile into the following two superposed parts: (i) the first part describes the skeleton shape of the entire profile; (ii) the second part describes the spatial change of a local gradient. Under this description, the preset profiles of $\tilde{\phi}_1$ and $\tilde{K}_f/\tilde{K}_f^{max}$ with $(1-\chi)/2$ and X^s capture only the first part of the physical profiles. The second part, although much smaller than the first part, is not considered in the above method. In physics the second part is closely associated with diffusion and more specifically diffusion coefficients. Therefore, to fine-tune the second part of a profile, we can multiply the corresponding diffusion coefficients obtained from the above method by a non-dimensional shape factor Π. For example, to slightly adjust the shape of the mass fraction profile, we can modify (3.75) to the following equation:

$$N_Y = 2\Pi N_L \frac{\varphi_1(r)}{\varphi_2(r)}. \tag{4.1}$$

Correspondingly, the $N_{e,h}$ should be updated with (3.76*a*,*b*). Consequently, the adjustment of the profile shape of the mass/volume fraction can also influence the turbulent kinetic energy profile. Therefore, we only need to adjust the value of the shape factor.

Based on the above analysis, for RANS profiles to approach physical results, we can adjust the first and second parts of the profiles. The first part can be achieved by adjusting the power index s for the turbulent kinetic energy profile. The second part can be achieved by adjusting the shape factor Π in (4.1). In principle, the values of s and Π can be determined with the experimental or numerical profiles of the volume fraction $\tilde{\phi}$ and turbulent kinetic energy $\tilde{K}_f$ at $A \to 0$. However, no smooth profile at $A \to 0$ can be obtained from the published literature. Hence, we have to determine their values using the smooth profiles at a larger A, such as the LES data produced by Kokkinakis *et al.* (2015). In figure 6 we plotted the variations of volume fraction profiles and re-normalised turbulent kinetic energy with power index s and shape factor Π. In the left figure we can see that the shape of the turbulent kinetic energy profile indeed varies with s, while the shape of the volume fraction profile is almost unchanged, as expected by the current theory. In the right figure we can see that the shape of both the volume fraction and turbulent kinetic energy profiles varies with Π, which is consistent with above analysis. Comparing the left and right figures, we find that the trend and degree of the variations are not similar. As for the degree of variation, the left figure shows that the profiles vary slightly with s, while the right figure shows that the profiles vary strongly with Π. As for the trend of variation, both figures show that the profile of the volume fraction becomes slower and shifts towards the same direction (right) with the increment of either Π or s. In contrast, the profile of

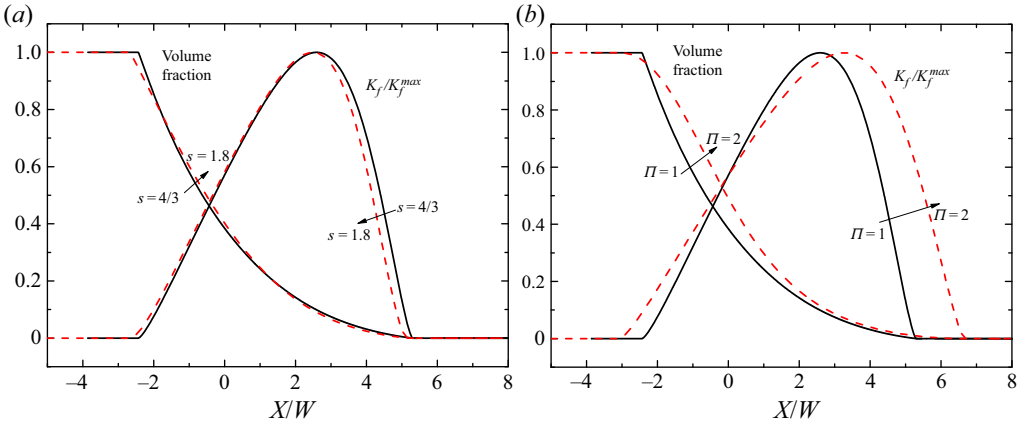

FIGURE 6. Variation of the profiles of the volume fraction of a heavy fluid $\tilde{\phi}_1$, re-normalised turbulent kinetic energy $\tilde{K}_f/\tilde{K}_f^{max}$ with power index s (a) and shape factor Π (b). The RANS results of the R–T test problem with $A = 0.9$ ($R = 20:1$) are calculated with a set of model coefficients determined by providing $\alpha_b = 0.05$, $\alpha_{KH} = 0.18$, $\theta = 0.25$, $\Delta E_k/\Delta PE = 0.5$, $\gamma = 1.4$, $C_D = 0.2$ and different s and Π. In the left figure the shape factor Π is fixed as 1, and s increases from 4/3 (black solid lines) to 1.8 (red dashed lines). In the right figure s is fixed as 4/3, and the shape factor Π increases from 1 (black solid lines) to 2 (red dashed lines).

the turbulent kinetic energy shifts towards the right and left direction corresponding to the increment of Π and s, respectively. Using the difference in variation trend and variation amplitude, one can always adjust s and Π to match the RANS results with the physical results. Figure 7 shows the comparison between the mixing evolution predicted by implicit LES (Youngs 2013; Kokkinakis *et al.* 2015) and current RANS simulations. The RANS evolutions are obtained by adjusting s and Π with the aforementioned logic to match the LES results. From the comparison, we can find that RANS profiles of both $\tilde{\phi}_1$ and $\tilde{K}_f/\tilde{K}_f^{max}$ almost coincide with LES profiles.

Up to now, we have successfully reproduced the spatial profile of physical evolution, as shown in figure 7. However, in this figure we can also see that the temporal scalings of RANS results has a slight deviation from that of LES results. This is because the initial input parameters influencing the temporal scalings (e.g. α_b, α_{KH}, θ, $\Delta E_k/\Delta PE$) have not been carefully determined. In fact, we can adjust the temporal scalings of the RANS results by adjusting the corresponding input parameters with the aid of relations derived in this paper. For example, the left graph of figure 7 shows that the RANS evolution of W (equivalently to h_b and α_b) is similar to implicit LES results, and the linear growth rate of $\tilde{K}_f^{max}$ (equivalently to α_K) of LES results is about 1.1 times of RANS results. Hence, according to (3.59), we only need to multiply the initial value of $\Delta E_k/\Delta PE$, i.e. 0.5, by 1.1 (which equals to 0.55). After considering this adjustment, the new RANS evolutions are compared with those of LES (Youngs 2013; Kokkinakis *et al.* 2015) in figure 8. From this figure we can see that RANS evolutions, either the temporal scalings or spatial profiles, almost completely coincide with those of LES results, validating the method developed above.

4.2. *Applications to various problems*

In § 4.1 we have demonstrated the process to determine a set of model coefficients with the constraint relations in § 3.2. From the procedures we can see that the determination

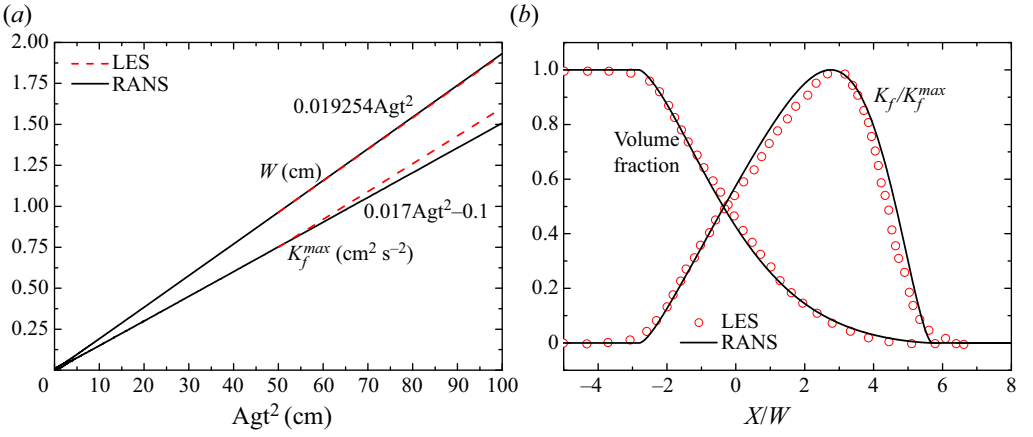

FIGURE 7. The comparison of the mixing evolution predicted by RANS (black lines) and implicit LES (Youngs 2013; Kokkinakis *et al.* 2015) (red dashed lines in the left figure and hollow red rings in the right figure). The left figure plots the evolution of integral mixing width W and maximum turbulent kinetic energy $\tilde{K}_f^{max}$ versus Agt^2, and the dashed lines show the corresponding linear growth rate of LES (Kokkinakis *et al.* 2015). The right figure plots the spatial profiles of the volume fraction of a heavy fluid $\tilde{\phi}_1$ and re-normalised turbulent kinetic energy $\tilde{K}_f/\tilde{K}_f^{max}$ versus re-normalised spatial coordinate X/W. The RANS results of the R–T test problem with $A = 0.9$ ($R = 20:1$) are calculated with a set of model coefficients determined by providing $\alpha_b = 0.05$, $\alpha_{KH} = 0.18$, $\theta = 0.25$, $\Delta E_k/\Delta PE = 0.5$, $\gamma = 1.4$, $C_D = 0.2$, $s = 1.6$ and $\Pi = 1.3$.

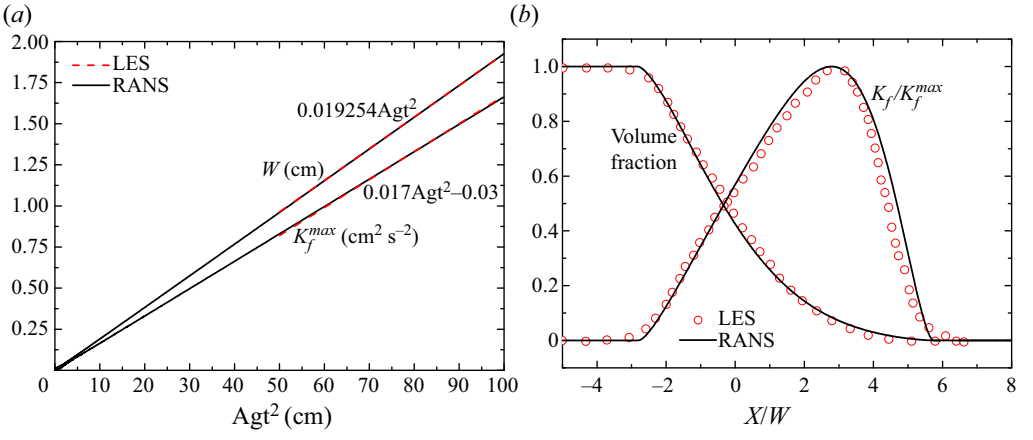

FIGURE 8. Comparison between RANS and LES ($\Delta E_k/\Delta PE = 0.55, A = 0.9$). For captions, see figure 7.

only needs physical evolution data of a specific problem. In § 4.1 the implicit LES data of R–T mixing at $A = 0.9$ are used. Based on these reliable data, we demonstrate that the final model coefficients can be determined by substituting the input parameters, $\alpha_b = 0.05$, $\alpha_{KH} = 0.18$, $\theta = 0.25$, $\Delta E_k/\Delta PE = 0.55$, $C_D = 0.2$, $s = 1.6$ and $\Pi = 1.3$, into (3.66)–(3.74), (4.1) and (3.76*a*,*b*). The corresponding values of model coefficients are listed in table 1. In practical applications, the problems involve R–T, R–M, K–H and reshocked R–M mixing synchronously, and the density ratio varies widely, as discussed

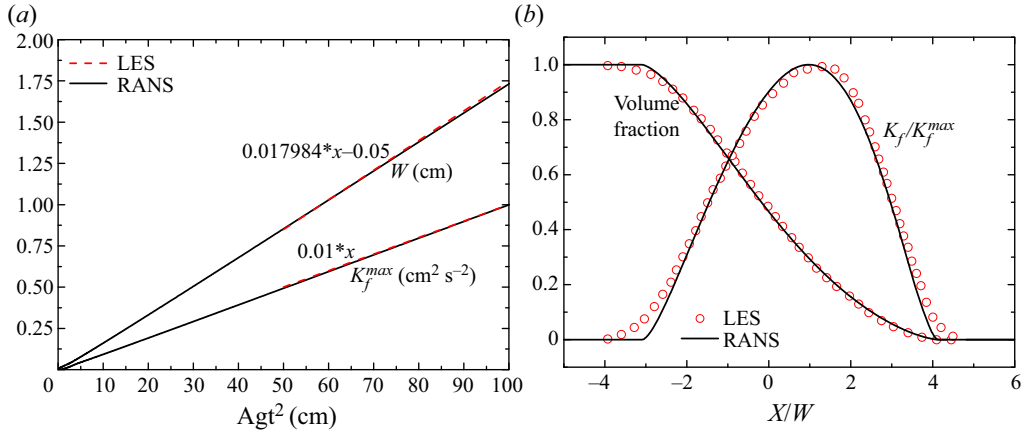

FIGURE 9. Comparison between RANS and LES ($\Delta E_k/\Delta PE = 0.55, A = 0.5$). For captions, see figure 7.

in the introduction. Therefore, it is necessary to show whether the model coefficients obtained in § 4.1 work for different problems and ratios or not. In this section we will apply the model coefficients determined for R–T mixing at $A = 0.9$ to other problems and density ratios, with detailed descriptions of problem configurations given in § 2.2. The results will show that such a set of model coefficients can be applied to different problems and density ratios.

Firstly, we demonstrate the applicability of the model coefficients to R–T mixing at different density ratios. In figure 9 we plot the comparison of the mixing evolutions predicted by LES (Youngs 2013; Kokkinakis *et al.* 2015) and RANS for R–T mixing at $A = 0.5$ ($R = 3:1$). Similar to the results shown in figure 8, the comparison shows that the evolution of either temporal scalings or spatial profiles of RANS results almost coincides with LES results. Up to now, the best solution is the RANS simulation conducted by Kokkinakis *et al.* (2015). In Kokkinakis *et al.* (2015) different model coefficients for $R = 3:1$ and $R = 20:1$ are used (see table 1) to best match the RANS with LES results. However, because of the lack of theoretical method about how to adjust the model coefficients, this study failed to match the evolution of mixing width W and turbulent kinetic energy $\tilde{K}_f^{max}$ simultaneously. In contrast, the method developed in this study not only successfully reproduces the evolution of temporal scalings or spatial profiles simultaneously, but what is more important is that this reproduction is for problems with different density ratios and the same set of model coefficients, highlighting its significance.

Next, the applicability of the same model coefficients for K–H mixing is demonstrated in figure 10. In this figure we plot the temporal evolution of total mixing width H, maximum turbulent length scale $\tilde{L}^{max}$ and maximum turbulent kinetic energy $\tilde{K}_f^{max}$. For this kind of mixing problem, the total mixing width $H(t)$ should grow linearly in time with a slope equal to $0.18\Delta\tilde{v}$, as discussed in § 2.1. As shown in figure 10, $H(t)$ grows linearly over time, with a slope of $0.18\Delta\tilde{v}$. Similarly, the maximum turbulent length scale $\tilde{L}^{max}$ also grows linearly with time, leading to a self-similar proportion constant β and validating the assumption of (3.9). The maximum turbulent kinetic energy $\tilde{K}_f^{max}$ approaches a constant value after a transient period of approximately 2 μs, consistent with physics and other RANS results (Chiravalle 2006). Unfortunately, for this case, no corresponding experimental or DNS data of $\tilde{K}_f$ is available for comparison. Moreover, it

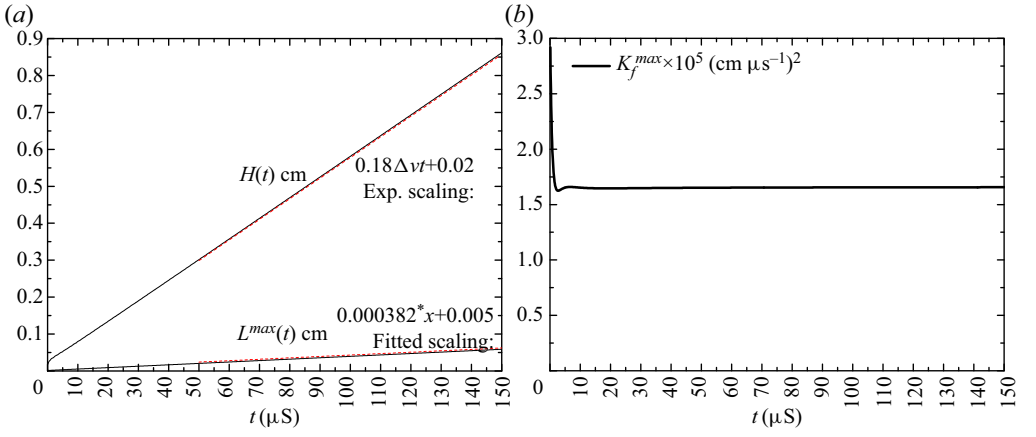

FIGURE 10. The temporal evolutions of total mixing width $H(t)$ (a), maximum turbulent eddy scale $\tilde{L}^{max}(t)$ (a) and maximum turbulent kinetic energy $\tilde{K}_f^{max}$ (b) with time t for K–H mixing. The solid lines denote the RANS results calculated with the same model coefficients as those of R–T mixing at $A = 0.9$. The red dashed lines in the left figure denote the temporal scalings.

is worth pointing out that Morgan, Schilling & Hartland (2018) found that it is difficult for k-L-type models to simultaneously match desired K–H turbulence intensity and growth rates. They successfully solved this problem by introducing an additional length scale equation. Noted that the improvement of the model closure form is beyond the scope of this paper, we recommend readers to read Morgan *et al.* (2018) for further details.

To further check whether the same set of model coefficients apply for classical R–M mixing or not, figure 11 shows the temporal evolutions of total mixing width, bubble mixing width and spike mixing width for classical R–M mixing at different density ratios, with the impact of shock on the interface from either a heavy ($A < 0$) or light ($A > 0$) fluid direction. Different from the classical R–T mixing problem, in classical R–M mixing, the nominal centre of mixed zones would move over time, resulting in a difficulty in quantifying the width of the bubble/spike mixing zone (i.e. $h_{b,s}$). To measure h_b/h_s of RANS results, in this paper we conduct a corresponding simulation with dense grids but without the K–L mixing model. Next, we use the result to determine the nominal evolution of material interface corresponding to $\tilde{\phi}_1 = 0.5$. Finally, the values of $h_{b,s}$ are determined by measuring the distance from the outer edge of the RANS mixing zone to the nominal material interface. Obviously, $h_{b,s}$ measured by this method is not strict, and errors may be introduced, especially at the early stage where $h_{b,s}$ is very small. For instance, at the early stage, we can see the unphysical phenomenon of $h_b > h_s$ in some subfigures of figure 11. However, in general, this method can effectively measure the physical $h_{b,s}$. From the log-log plots in figure 11 we can see that all RANS results successfully produce the power scaling of $h_{b,s} \propto t^{\theta_{b,s}}$, with $\theta_b \sim 0.25$ and $\theta_s \geq \theta_b$ for all cases. This can be more clearly shown in figure 12, which directly plots the comparison of θ_b and θ_s between the present results at $A = \pm 0.1, \pm 0.5, \pm 0.9$ and the LEM experimental measurements (Dimonte & Schneider 2000). It reveals that $\theta_s \approx \theta_b$ at small Atwood number ($|A| \leq 0.5$) and $\theta_s > \theta_b$ at larger Atwood number, where the mixing grows asymmetrically. These results agree very well with the existing numerical simulations and experiments (Dimonte & Schneider 2000; Zhou 2017*b*), validating the effectiveness of the current method for classical R–M problems.

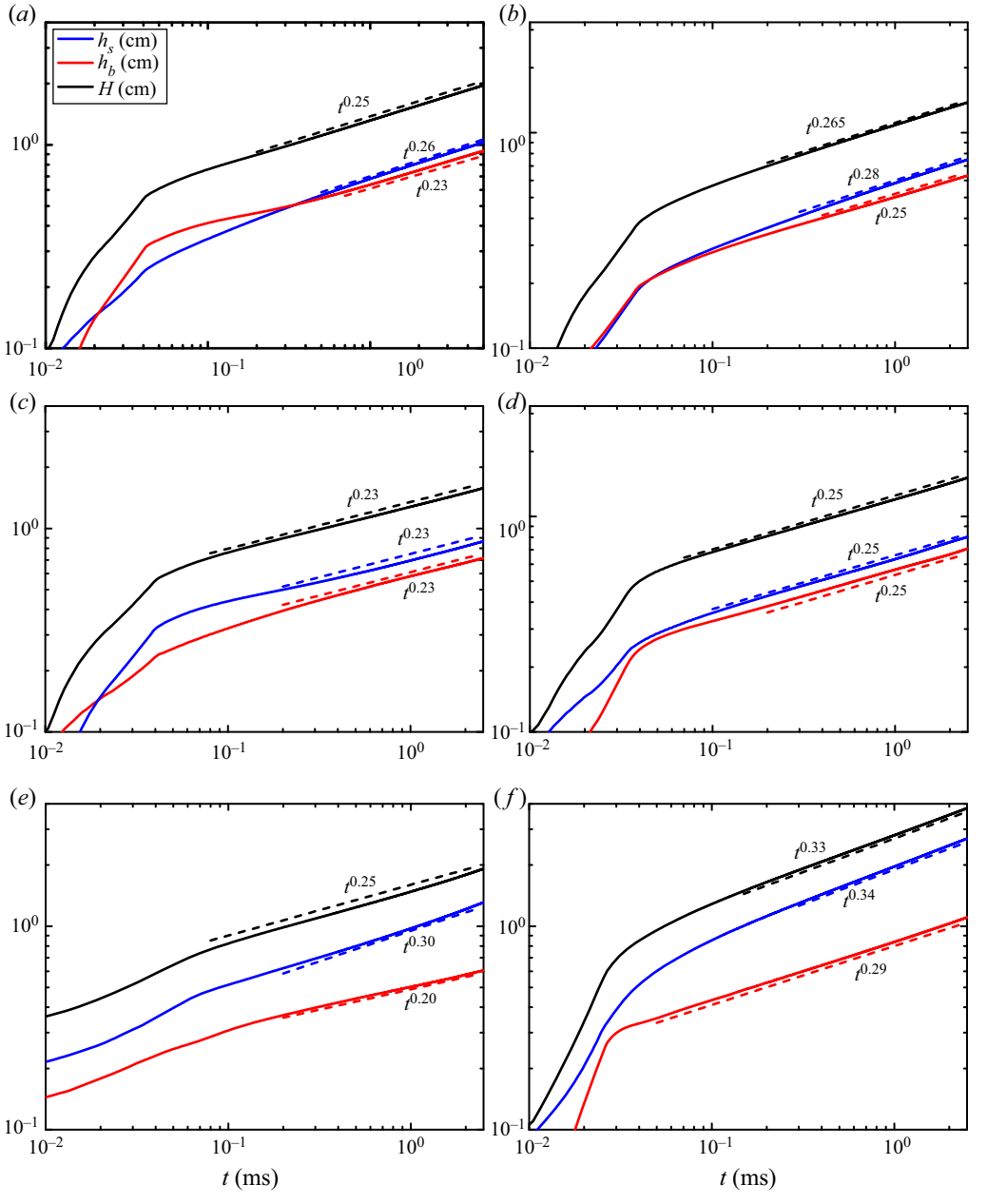

FIGURE 11. The temporal evolutions of the total mixing width $H(t)$ (black lines), bubble mixing width $h_b(t)$ (red lines) and spike mixing width $h_s(t)$ (blue lines) of classical R–M mixing at (*a*) $A = 0.1$, (*b*) $A = -0.1$, (*c*) $A = 0.5$, (*d*) $A = -0.5$, (*e*) $A = 0.9$ and (*f*) $A = -0.9$. The solid lines denote the RANS results calculated with the same model coefficients as those of R–T mixing at $A = 0.9$. The dashed lines denote the fitted temporal scalings.

The above examples demonstrate the applicability of the same model coefficients for a single mixing phenomenon. As discussed in the introduction, practical applications generally involve R–T, R–M and K–H mixing phenomena synchronously. As we discussed in § 2.1, the reshocked R–M mixing is just such an example. Hence, we use this problem

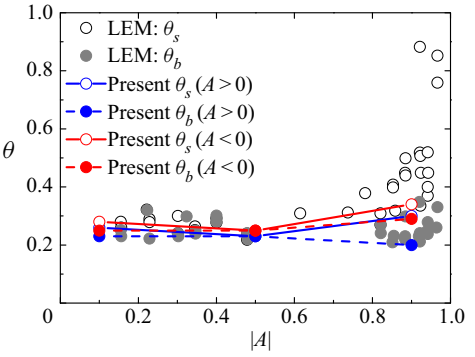

FIGURE 12. Comparison of θ_b and θ_s between the present results at $A = \pm 0.1, \pm 0.5, \pm 0.9$ and LEM experiments (Dimonte & Schneider 2000).

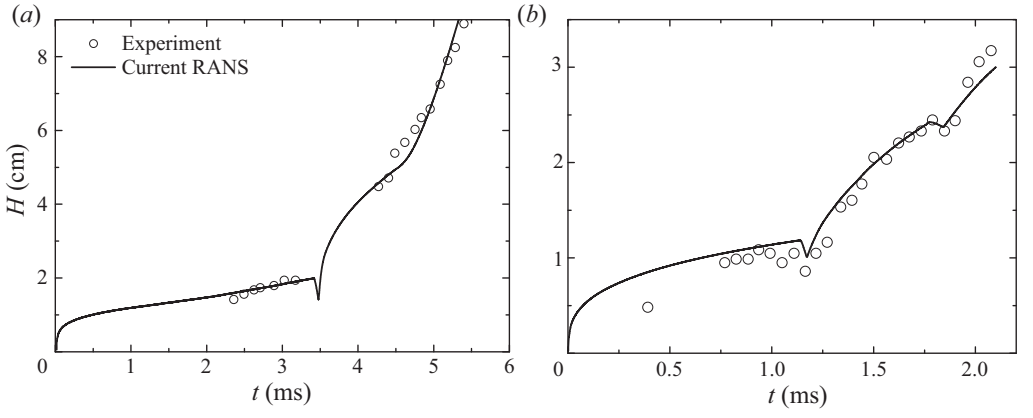

FIGURE 13. The temporal evolutions of the total mixing width $H(t)$ of reshocked R–M mixing problem with (*a*) $A = 0.67$ and (*b*) $A = -0.67$. The solid lines denote the RANS results calculated with the same model coefficients as those of R–T mixing at $A = 0.9$. The symbols denote the experiment results conducted by Vetter & Sturtevant (1995) (*a*) and Poggi *et al.* (1998) (*b*). See Xiao *et al.* (2020) for more details.

to comprehensively examine the effectiveness of the same set of model coefficients for complex problems. The RANS results are plotted in figure 13 and compared with the measurements of corresponding experiments. From the comparisons, we can see that the temporal evolution of the total mixing width highly coincides with that of experimental results, with the impact of shock on the interface from either a light ($A = 0.67$) or heavy ($A = -0.67$) fluid direction. In fact, predicting mixing width evolution with the RANS model has been conducted by many researchers (Dimonte & Tipton 2006; Zhou 2017*b*; Moran-Lopez & Schilling 2013). To the best of our knowledge, with the same set of model coefficients, no study can successfully reproduce the reshocked R–M experiments conducted by Vetter & Sturtevant (1995) ($A > 0$) and Poggi *et al.* (1998) ($A < 0$) at the same time, especially with such a good degree of collapse. A more comprehensive validation of the set of parameters on reshocked R–M problems can be found in our recent paper (Xiao *et al.* 2020).

In short, all the above examples demonstrate the possibility of using the same RANS model coefficients for mixing problems involving different configurations, density ratios and physical quantities.

5. Discussions

As mentioned in the introduction, a turbulence model includes two aspects: physical modelling and model coefficients. The accurate prediction of mixing evolution with the RANS model needs a precondition that both parts are correct. In this paper we only consider the determination of model coefficients, and document all details of the current method. To demonstrate this method, constraint relations and model coefficients are derived with an example of a K–L turbulence model. Essentially, what we present in this paper is a methodology. The most important matter is not the final values of the model coefficients but the ideas hidden behind the determination of model coefficients, along with detailed reasons explained as follows.

Recalling the procedure of the current method in determining model coefficients, we can find that the values of the model coefficients are essentially coupled with physical modelling itself. If we modify physical modelling to achieve our expectation of $\boldsymbol{F}_{RANS} \rightarrow \boldsymbol{F}_{phy}$, we have to adjust some model coefficients, although it is possible that sometimes the magnitude of this adjustment is negligible. However, the current method implies that this step, in principle, is necessary, and it gives a theoretical guidance on how to adjust the model coefficients step by step. Taking the modelling of turbulent diffusion of total energy D_E as a specific example, D_E is modelled as $\nabla \cdot [(\mu_t/N_h)\nabla\tilde{e}]$ and $\nabla \cdot [(\mu_t/N_h)\nabla\tilde{h}]$ in Dimonte & Tipton (2006) and Kokkinakis *et al.* (2015), respectively. Applying the current method to the two physical models, we can derive that the corresponding model coefficients should meet the relation of $N_h = \gamma N_e$, derived from (3.65*a*,*b*). As a consequence, without considering the rationality of physical modelling itself, different physical modelling can give the same RANS results when matched model coefficients are used correspondingly. This will improve our understanding about the influence of different modelling on the RANS results. For example, in Kokkinakis *et al.* (2015) the influence of different modelling of D_E on RANS results is estimated under the same value of $N_h = N_e$, while the current study suggests that in such a comparison it is more appropriate using $N_h = \gamma N_e$. Considering this dependence of model coefficients on physical modelling, when a new or improved RANS model is developed, we suggest that the methodology and procedures documented in this paper should always be executed to determine a set of corresponding model coefficients. In fact, our recent work on the k-ϵ model also validates this methodology, and the derived set of model coefficients is proven to be applicable to the tested benchmark cases here. This work will be presented and discussed in the near future.

Moreover, even for a deterministic model, a set of universal model coefficients for all problems does not exist. Considering the K–L mixing model given in this paper as an example, the current method shows that the model coefficients are determined by the input parameters – α_b, α_{KH}, θ, $\Delta E_k/\Delta PE$, s, γ and C_D. Naturally, for different input parameters, the model coefficients are different. Here, we briefly discuss two situations. The first situation is associated with initial perturbations. As we discussed in § 2.1, in physics α_b and θ depend on initial perturbations (Dimonte 2004; Ramaprabhu *et al.* 2005; Livescu *et al.* 2011; Youngs 2013). In this paper the values, $\alpha_b = 0.05$ and $\theta = 0.25$, are given by referring to the LEM experiments (Dimonte & Schneider 2000). For perturbations composed entirely of short waves, the corresponding $\alpha_b \approx 0.025$ (Dimonte *et al.* 2004) should be used. Similarly, for K–H mixing, the growth rate $\alpha_{KH} = 0.18$ should be changed for experiments different from Brown & Roshko (1974), such as experiments conducted by Bell & Mehta (1990) ($\alpha_{KH} \sim 0.08$). It also shows that an additional degree of freedom should be added for Bell & Mehta (1990) experiments, as discussed by Morgan *et al.* (2018). Therefore, our work implies that there does not exist a set of universal model

coefficients for all problems; what exists for all problems are the constraint relations derived from the current methodology, e.g. (3.66)–(3.74), (4.1) and (3.76*a*,*b*). The second situation is associated with the fluid property γ. According to (3.65*a*,*b*), γ will influence the value of N_e. For two fluids with the same γ, the value of N_e will vary according to the changing values of γ and can be determined using (3.65*a*,*b*). For two fluids with different γ, such as the reshocked R–M mixing investigated in this study, the situation becomes complex. Because of the lack of a constant γ across the mixing zone, it is impossible to obtain a constant N_e with (3.65*a*,*b*). Therefore, in this paper we prefer to model D_E as $D_E = \nabla \cdot [(\mu_t/N_h)\nabla\tilde{h}]$, instead of $D_E = \nabla \cdot [(\mu_t/N_e)\nabla\tilde{e}]$. If the latter model was used, we suggest using a varied N_e according to (3.65*a*,*b*), in which γ is treated as the spatial-dependent heat ratio of the mixture, i.e. $\gamma \equiv \bar{p}/\bar{\rho}\tilde{e} + 1$.

6. Conclusions

In the foreseeable future the prediction of mixing with a RANS model will remain a priority for engineering applications. Over the past several decades, although considerable efforts have been made to improve the turbulence mixing model, the uncertainty in determining model coefficients still challenges the academic community. During this period, Dimonte and Tipton's method significantly advanced the determination of model coefficients. This method is established on a very specific assumption on the shape of the mixing profile. Unfortunately, this assumption was later found to be inconsistent with reliable numerical simulations. In this paper, based on our understanding of Dimonte and Tipton's work, we give up the assumption on the specific shape of the mixing profile. Instead, we only assume that the mixing profile meets a certain type of shape. Moreover, inspired by the idea of Reynolds decomposition, the RANS evolution has been segmented into two parts. Based on our knowledge of the mixing problems, the main part is formulated *a priori* in the form of separated temporal–spatial variables. After substituting the formulations into the RANS equation, a critical idea of integrating the RANS equation across the mixing zone has been introduced, yielding a set of approximate constraint relations among model coefficients.

By fully using the derived constraint relations, the values of the model coefficients can be accurately determined with only three steps in the following order to produce $\boldsymbol{F}_{RANS} \rightarrow \boldsymbol{F}_{phy}$: (i) determine the drag coefficient C_D with the additional requirement that a set of model coefficients should be appropriate for arbitrary density ratios; (ii) reproduce the physical spatial profiles by adjusting the shape factor; (iii) reproduce the physical temporal scalings by adjusting some growth law associated input parameters. The above order is determined because the adjustment of the shape factor does not significantly affect the evolution of temporal scalings (such as the realised α_b and $\Delta E_k/\Delta PE$), and, thus, we do not suggest to change the order arbitrarily. Using the same set of model coefficients determined with the above steps, the K–L model successfully reproduces the physical evolutions of mixing problems, in terms of different physical quantities (e.g. temporal scalings and spatial profiles), density ratios and different problems (R–T, R–M, K–H and reshocked R–M).

Finally, in this paper the K–L mixing model is just used as an example to elaborate key ideas and procedures. According to the discussions in § 5, we can conclude that the most important thing in this paper is the methodology and not the specific values of the model coefficients. It is possible to apply the current method to other mixing models and turbulence models with self-similar evolutions.

Acknowledgements

This research was supported by the National Natural Science Foundation of China (NSFC) under grant numbers 11972093 and 91852207, and by the China Postdoctoral Science Foundation under grant number 2020M670228. The authors want to thank Dr H.-F. Li, Dr Z.-X. Hu, Dr L. Li and Dr K. Xue for their helpful insights, Dr W.-D. Ni for helpful English editing assistance and anonymous referees for their professional comments, which have greatly improved the quality of this paper.

Declaration of interests

The authors report no conflict of interest.

REFERENCES

AKULA, B. & RANJAN, D. 2016 Dynamics of buoyancy-driven flows at moderately high Atwood numbers. *J. Fluid Mech.* **795**, 313–355.

ANDEREWS, M. J. & SPALDING, D. B. 1990 A simple experiment to investigate 2-dimensional mixing by Rayleigh–Taylor instability. *Phys. Fluids* **2** (6), 922–927.

BANERJEE, A. & ANDREWS, M. J. 2009 3D simulations to investigate initial condition effects on the growth of Rayleigh–Taylor mixing. *Intl J. Heat Mass Transfer* **52** (17), 3906–3917.

BELL, J. H. & MEHTA, R. D. 1990 Development of a two-stream mixing layer from tripped and untripped boundary layers. *AIAA J.* **28** (12), 2034–2042.

BROWN, G. L. & ROSHKO, A. 1974 On density effects and large structure in turbulent mixing layers. *J. Fluid Mech.* **64** (4), 775–816.

BURROWS, A. 2000 Supernova explosions in the universe. *Nature* **403** (6771), 727–733.

CABOT, W. & ZHOU, YE 2013 Statistical measurements of scaling and anisotropy of turbulent flows induced by Rayleigh–Taylor instability. *Phys. Fluids* **25** (1), 15107.

CABOT, W. H. & COOK, A. W. 2006 Reynolds number effects on Rayleigh–Taylor instability with possible implications for type-Ia supernovae. *Nat. Phys.* **2** (8), 562–568.

CHIRAVALLE, V. P. 2006 The k-L turbulence model for describing buoyancy-driven fluid instabilities. *Laser Part. Beams* **24** (3), 381–394.

CLARK, T. T. & ZHOU, Y. 2003 Self-similarity of two flows induced by instabilities. *Phys. Rev.* E **68** (6), 066305.

COOK, A. W. & CABOT, W. H. 2006 Reynolds number effects on Rayleigh–Taylor instability with possible implications for type Ia supernovae. *Nat. Phys.* **2** (8), 562–568.

DIMONTE, G. 2000 Spanwise homogeneous buoyancy-drag model for Rayleigh–Taylor mixing and experimental evaluation. *Phys. Plasmas* **7** (6), 2255–2269.

DIMONTE, G. 2004 Dependence of turbulent Rayleigh–Taylor instability on initial perturbations. *Phys. Rev.* E **69** (5), 056305.

DIMONTE, G. & SCHNEIDER, M. 2000 Density ratio dependence of Rayleigh–Taylor mixing for sustained and impulsive acceleration histories. *Phys. Fluids* **12** (2), 304–321.

DIMONTE, G. & TIPTON, R. 2006 *K-L* turbulence model for the self-similar growth of the Rayleigh–Taylor and Richtmyer–Meshkov instabilities. *Phys. Fluids* **18** (8), 085101.

DIMONTE, G., YOUNGS, D. L., DIMITS, A., WEBER, S., MARINAK, M., WUNSCH, S., GARASI, C., ROBINSON, A., ANDREWS, M. J., RAMAPRABHU, P., *et al.* 2004 A comparative study of the turbulent Rayleigh–Taylor instability using high-resolution three-dimensional numerical simulations: the alpha-group collaboration. *Phys. Fluids* **16** (5), 1668–1693.

GAO, F., HE, Z., ZHANG, Y., LI, L. & TIAN, B. 2017 The characteristic of turbulent mixing at late stage of the Richtmyer–Meshkov instability. *AIP Adv.* **7** (7), 075020.

GAO, F., ZHANG, Y., HE, Z. & TIAN, B. 2016 Formula for growth rate of mixing width applied to Richtmyer–Meshkov instability. *Phys. Fluids* **28** (11), 114101.

HARTEN, A. 1997 High resolution schemes for hyperbolic conservation laws. *J. Comput. Phys.* **135** (2), 260–278.

HARTEN, A., LAX, P. D. & LEER, B. V. 1983 On upstream differencing and Godunov-type schemes for hyperbolic conservation laws. *SIAM Rev.* **25** (1), 35–61.

HELMHOLTZ, V. 1868 On discontinuous movements of fluids. *Lond. Edinb. Dubl. Phil. Mag. J. Sci.* **36** (244), 337–346.

KELVIN, L. 1871 Hydrokinetic solutions and observations. *Lond. Edinb. Dubl. Phil. Mag. J. Sci.* **42** (281), 362–377.

KIM, K. H. & KIM, C. 2005*a* Accurate, efficient and monotonic numerical methods for multi-dimensional compressible flows. Part I: spatial discretization. *J. Comput. Phys.* **208** (2), 527–569.

KIM, K. H. & KIM, C. 2005*b* Accurate, efficient and monotonic numerical methods for multi-dimensional compressible flows. Part II: multi-dimensional limiting process. *J. Comput. Phys.* **208** (2), 570–615.

KOKKINAKIS, I. W., DRIKAKIS, D. & YOUNGS, D. L. 2019 Modeling of Rayleigh–Taylor mixing using single-fluid models. *Phys. Rev.* E **99** (1), 013104.

KOKKINAKIS, I. W., DRIKAKIS, D., YOUNGS, D. L & WILLIAMS, R. J. R. 2015 Two-equation and multi fluid turbulence models for Rayleigh–Taylor mixing. *Intl J. Heat Fluid Flow* **56**, 233–250.

KRIVETS, V. V., FERGUSON, K. J. & JACOBS, J. W. 2017 Turbulent mixing induced by Richtmyer–Meshkov instability. *AIP Conf. Proc.* **1793** (1), 1–4.

LI, H., HE, Z. W., ZHANG, Y. S. & TIAN, B. L. 2019*a* Growth law of reshocked Richtmyer–Meshkov mixing width. *J. Fluid Mech.* (submitted).

LI, H., HE, Z. W., ZHANG, Y. S. & TIAN, B. L. 2019*b* On the role of rarefaction/compression waves in Richtmyer–Meshkov instability with reshock. *Phys. Fluids* **31** (5), 54102.

LIU, H. & XIAO, Z. 2016 Scale-to-scale energy transfer in mixing flow induced by the Richtmyer–Meshkov instability. *Phys. Rev.* E **93** (5), 053112.

LIVESCU, D. 2013 Numerical simulations of two-fluid turbulent mixing at large density ratios and applications to the Rayleigh–Taylor instability. *Phil. Trans. R. Soc. Lond.* A **371** (2003), 20120185.

LIVESCU, D., WEI, T. & PETERSEN, M. R. 2011 Direct numerical simulations of Rayleigh–Taylor instability. *J. Phys.: Conf. Ser.* **318** (8), 082007.

MESHKOV, E. E. 1969 Instability of the interface of two gases accelerated by a shock wave. *Fluid Dyn.* **4** (5), 101–104.

MORAN-LOPEZ, J. T. & SCHILLING, O. 2013 Multicomponent Reynolds-averaged Navier–Stokes simulations of reshocked Richtmyer–Meshkov instability-induced mixing. *High Energ. Dens. Phys.* **9** (1), 112–121.

MORGAN, B. E. 2018 Response to 'Comment on "Large-eddy simulation and unsteady RANS simulations of a shock-accelerated heavy gas cylinder" by B. E. Morgan, J. Greenough'. *Shock Waves* **28** (6), 1301–1302.

MORGAN, B. E. & GREENOUGH, J. A. 2016 Large-eddy and unsteady RANS simulations of a shock-accelerated heavy gas cylinder. *Shock Waves* **26**, 355–383.

MORGAN, B. E, SCHILLING, O. & HARTLAND, T. A. 2018 Two-length-scale turbulence model for self-similar buoyancy-, shock-, and shear-driven mixing. *Phys. Rev.* E **97** (1), 013104.

MUESCHKE, N. J. & SCHILLING, O. 2009 Investigation of Rayleigh–Taylor turbulence and mixing using direct numerical simulation with experimentally measured initial conditions. I. Comparison to experimental data. *Phys. Fluids* **21** (1), 14106.

OLSON, D. H. & JACOBS, J. W. 2009 Experimental study of Rayleigh–Taylor instability with a complex initial perturbation. *Phys. Fluids* **21** (3), 34103.

POGGI, F., THOREMBEY, M.-H. & RODRIGUEZ, G. 1998 Velocity measurements in turbulent gaseous mixtures induced by Richtmyer–Meshkov instability. *Phys. Fluids* **10** (11), 2698–2700.

RAMAPRABHU, P., DIMONTE, G. & ANDREWS, M. J. 2005 A numerical study of the influence of initial perturbations on the turbulent Rayleigh–Taylor instability. *J. Fluid Mech.* **536**, 285–319.

RAYLEIGH, LORD 1882 Investigation of the character of the equilibrium of an incompressible heavy fluid of variable density. *Proc. Lond. Math. Soc.* **201** (1), 170–177.

READ, K. I. 1984 Experimental investigation of turbulent mixing by Rayleigh–Taylor instability. *Physica* D **12** (1–3), 45–58.

RICHTMYER, R. D. 1960 Taylor instability in shock acceleration of compressible fluids. *Commun. Pure. Appl. Maths* **13** (2), 297–319.

ROBERTS, M. S. & JACOBS, J. W. 2016 The effects of forced small-wavelength, finite-bandwidth initial perturbations and miscibility on the turbulent Rayleigh–Taylor instability. *J. Fluid Mech.* **787**, 50–83.

RUAN, Y. C., ZHANG, Y. S., TIAN, B. L. & ZHANG, X. T. 2019 Density-ratio-invariant mean-species-profile of classical Rayleigh–Taylor mixing. *Phys. Rev. Fluids* (submitted).

SLESSOR, M. D., ZHUANG, M. & DIMOTAKIS, P. E. 2000 Turbulent shear-layer mixing: growth-rate compressibility scaling. *J. Fluid Mech.* **414**, 35–45.

SWEBY, P. K. 1984 High resolution schemes using flux limiters for hyperbolic conservation laws. *SIAM J. Numer. Anal.* **21** (5), 995–1011.

TAYLOR, G. 1950 The instability of liquid surfaces when accelerated in a direction perpendicular to their planes. I. *Proc. R. Soc. Lond.* A **201** (1065), 192.

THOMAS, V. A. & KARES, R. J. 2012 Drive asymmetry and the origin of turbulence in an ICF implosion. *Phys. Rev. Lett.* **109** (7), 075004.

THORNBER, B., DRIKAKIS, D., WILLIAMS, R. J. R. & YOUNGS, D. 2008*a* On entropy generation and dissipation of kinetic energy in high-resolution shock-capturing schemes. *J. Comput. Phys.* **227** (10), 4853–4872.

THORNBER, B., DRIKAKIS, D., YOUNGS, D. L. & WILLIAMS, R. J. R. 2010 The influence of initial conditions on turbulent mixing due to Richtmyer–Meshkov instability. *J. Fluid Mech.* **654**, 99–139.

THORNBER, B., GROOM, M. & YOUNGS, D. 2018 A five-equation model for the simulation of miscible and viscous compressible fluids. *J. Comput. Phys.* **372**, 256–280.

THORNBER, B., MOSEDALE, A., DRIKAKIS, D., YOUNGS, D. & WILLIAMS, R. J. R. 2008*b* An improved reconstruction method for compressible flows with low Mach number features. *J. Comput. Phys.* **227** (10), 4873–4894.

TORO, E. F., SPRUCE, M. & SPEARES, W. 1994 Restoration of the contact surface in the HLL-Riemann solver. *Shock Waves* **4** (1), 25–34.

TRITSCHLER, V. K., ZUBEL, M., HICKEL, S. & ADAMS, N. A. 2014 Evolution of length scales and statistics of Richtmyer–Meshkov instability from direct numerical simulations. *Phys. Rev.* E **90** (6), 063001.

VETTER, M. & STURTEVANT, B. 1995 Experiments on the Richtmyer–Meshkov instability of an air/SF6 interface. *Shock Waves* **4** (5), 247–252.

XIAO, M., ZHANG, Y. & TIAN, B. 2020 Unified prediction of reshocked Richtmyer–Meshkov mixing with K-L model. *Phys. Fluids* **32** (3), 032107.

YOUNGS, D. L. 1989 Modelling turbulent mixing by Rayleigh–Taylor instability. *Physica* D **37** (1–3), 270–287.

YOUNGS, D. L. 2013 The density ratio dependence of self-similar Rayleigh–Taylor mixing. *Phil. Trans. R. Soc. Lond.* A **371** (2003), 20120173.

YOUNGS, D. L. 2017 Rayleigh–Taylor mixing: direct numerical simulation and implicit large eddy simulation. *Phys. Scr.* **92** (7), 074006.

ZHANG, Y.-S. 2018 Comment on 'Large-eddy and unsteady RANS simulations of a shock-accelerated heavy gas cylinder' by B. E. Morgan, J. Greenough. *Shock Waves* **28** (6), 1299–1300.

ZHANG, Y.-S., HE, Z.-W., GAO, F.-J., LI, X.-L. & TIAN, B.-L. 2016 Evolution of mixing width induced by general Rayleigh–Taylor instability. *Phys. Rev.* E **93** (6), 063102.

ZHANG, Y.-S., RUAN, Y.-C., XIE, H.-S. & TIAN, B.-L. 2020 Mixed mass of classical Rayleigh–Taylor mixing at arbitrary density ratios. *Phys. Fluids* **32** (1), 011702.

ZHOU, Y. 2017*a* Rayleigh–Taylor and Richtmyer–Meshkov instability induced flow, turbulence, and mixing. I. *Phys. Rep.* **720–722** (C), 1–136.

ZHOU, Y. 2017*b* Rayleigh–Taylor and Richtmyer–Meshkov instability induced flow, turbulence, and mixing. II. *Phys. Rep.* **723–725**, 1–160.

ZHOU, Y., CABOT, W. H. & THORNBER, B. 2016 Asymptotic behavior of the mixed mass in Rayleigh–Taylor and Richtmyer–Meshkov instability induced flows. *Phys. Plasmas* **23** (5), GO5.012.

ZHOU, Z.-R., ZHANG, Y.-S. & TIAN, B.-L. 2018 Dynamic evolution of Rayleigh–Taylor bubbles from sinusoidal, w-shaped, and random perturbations. *Phys. Rev.* E **97** (3), 033108.